Pyrolysis of ethanol studied in a new high-repetition-rate shock tube coupled to synchrotron-based double imaging photoelectron/photoion coincidence spectroscopy

S Nagaraju, R S Tranter, F E Cano Ardila, S Abid, P T Lynch, G A Garcia, J F Gil, L Nahon, N Chaumeix, A Comandini

Combustion and Flame 226 (2021) 53–68

Contents lists available at ScienceDirect

Combustion and Flame

journal homepage: www.elsevier.com/locate/combustflame

Pyrolysis of ethanol studied in a new high-repetition-rate shock tube coupled to synchrotron-based double imaging photoelectron/photoion coincidence spectroscopy

S. Nagaraju[a], R.S. Tranter[b], F.E. Cano Ardila[a], S. Abid[a,c], P.T. Lynch[d], G.A. Garcia[e], J.F. Gil[e], L. Nahon[e], N. Chaumeix[a], A. Comandini[a,*]

[a] CNRS-INSIS, I.C.A.R.E., 1C Avenue de la recherche scientifique, 45071 Orléans cedex 2, France
[b] Chemical Sciences and Engineering Department, Argonne National Laboratory, 9700 S. Cass Avenue, Lemont, Illinois 60439, USA
[c] Université d'Orléans, 6 Avenue du Parc Floral, 45100 Orléans, France
[d] Department of Mechanical and Industrial Engineering, University of Illinois at Chicago, 842 W. Taylor Street, Chicago, Illinois 60607, USA
[e] Synchrotron SOLEIL, L'Orme des Merisiers, St. Aubin BP 48, 91192 Gif sur Yvette, France

ARTICLE INFO

Article history:
Received 31 August 2020
Revised 20 November 2020
Accepted 20 November 2020

Keywords:
High-repetition-rate shock tube
Synchrotron
Photoelectron photion coincidence
Chemical kinetics
Pyrolysis
Ethanol
Photoelectron spectra
Mass spectra
Species profiles

ABSTRACT

Shock tube techniques for kinetic studies are continuously evolving driven by advances in kinetic modeling and detection techniques. An innovative category of shock tubes has been recently developed for use at Synchrotron facilities. In this work, a new high-repetition-rate shock tube (HRRST) was constructed to employ synchrotron-based double imaging photoelectron/photoion coincidence spectroscopy (i^{2}PEPICO) at the beamline DESIRS of the SOLEIL synchrotron. The shock tube design and performance (pressure profiles, repeatability of operations) are presented for the first time together with the detailed description of the coupling with the molecular beam end-station holding the i^{2}PEPICO spectrometer. The first experimental results with the HRRST/i^{2}PEPICO on ethanol pyrolysis are grouped based on four different experimental conditions, each highlighting functionality of this novel experimental system. Experiments were performed at temperatures between 1232 K and 1525 K, pressures between 6.2 bar and 7.5 bar, with 2.7% or 0.25% ethanol in argon, and photon energy of 10.0 eV or 11.0 eV. The results are supported by kinetic analyses with the CRECK model. This study shows the potential of the HRRST/i^{2}PEPICO combination for obtaining detailed mechanistic and kinetic data for complex chemical systems. Mass spectra, photoelectron spectra and time-resolved species profiles were obtained for a wide variety of species from methyl radicals to large polyaromatic hydrocarbons. The different experimental conditions studied indicate how future experiments can be designed to target key regimes facilitating the elucidation of desired kinetic and mechanistic data.

1. Introduction

In 1899, Vieille published the progenitor of modern shock tubes [1,2], which have subsequently provided much of the experimental data on high-temperatures gas-phase chemistry. These extremely versatile instruments have been designed for a wide variety of kinetic and mechanistic studies, see for examples refs. [3,4] and are particularly useful for studying fast, elementary reactions and targeted subsets of complex chemical systems. One of the principle features of shock tubes that facilitates high temperature studies is their ability to nearly instantaneously generate, in a controlled fashion, almost any combination of pressure and temperature of practical interest. Studies have been performed from a few Torr and several hundred Kelvin [5,6] through hundreds of atmospheres and thousands of Kelvin [7].

During the last sixty years, there have been many creative developments in the design of shock tubes for gas phase chemical kinetic studies and the diagnostics used with them. In particular, in recent years some of the most notable developments in techniques include: very long observation periods [8], very high pressures [9,10], studies of non-volatile complex fuels [11], measurements of dP/dt for accurate interpretation of ignition delay times [12,13]. These methods have facilitated a broad range of studies that were previously unattainable and/or improved their accuracy. However, these techniques are all essentially single-shot experiments, and

* Corresponding author.
E-mail address: andrea.comandini@cnrs-orleans.fr (A. Comandini).

https://doi.org/10.1016/j.combustflame.2020.11.035
0010-2180/

it would be challenging to perform signal averaging over multiple experiments to improve the signal to noise ratio (S/N). Techniques have also been developed to create reproducible reaction conditions in shock tubes reliably and efficiently [14,15] permitting signal averaging [16] to improve the S/N of weak signals. Recently, a new class of shock tubes, miniature high repetition rate shock tubes (HRRST), has been developed to exploit the capabilities of synchrotron-based diagnostics [17]. Traditionally, synchrotron methods for chemical kinetics have been restricted to pseudo-steady state reactors such as flow tubes [18] and low-pressure flames [19] where signal averaging is easily applied to obtain sufficient S/N from the inherently weak signals. HRRSTs were designed to be small enough to fit into the restricted space at synchrotron facilities, give reproducible reaction conditions and have a sufficiently high firing rate to make efficient use of limited synchrotron time. To date HRRSTs have been used with *X*-ray diagnostics at the Advanced Photon Source (Argonne National Laboratory) to probe boundary layers and gas states [17,20] and vacuum ultra violet photoionization mass spectrometry (VUV-PIMS) at the Advanced Light Source (Lawrence Berkeley National Laboratory) to explore reaction mechanisms [21–23].

The complement to the shock tube for chemical kinetics is the diagnostic equipment to probe the chemical reactions. To study complex chemical systems, it is often desirable to be able to simultaneously monitor a large number of species including radicals. Such measurements have been made of several key combustion species by optical spectroscopy [24,25]. However, often a separate laser source is required for each species. Furthermore, each optical probe has different sensitivities and detection limits which place practical limits on the number of species that can be monitored. Shock tubes coupled to time-of-flight mass spectrometers can detect a broad range of stable and radical species simultaneously [26–29]. Typically, lab-based systems use electron ionization, which has the advantage of producing strong signals but at the expense of fragmentation in the ionization process which complicates interpretation of the mass spectra. Photoionization, as used in references [19,21–23] typically reduces fragmentation compared to electron ionization resulting in cleaner mass spectra. However, the signal levels are typically much lower, and averaging over many experiments is necessary; although with an HRRST this is feasible with highly tunable, narrow bandwidth, synchrotron VUV one can obtain the photoionization spectrum of a species as well as the mass from a HRRST/VUV-PIMS experiment. The photoionization spectrum is similar to a fingerprint of the molecule and permits positive identification of species. Of particular value is that species of the same nominal mass (e.g. H_2CO, C_2H_6 and NO [23]), and isomers (see for example ref [19]) can be distinguished by their photoionization spectra. Furthermore, a measured photoionization spectrum can be decomposed into a linear combination of spectra from a mixture of molecules and isomers allowing contributions to a single mass peak to be assigned to discrete species. VUV-PIMS experiments are very informative for unravelling complex mechanisms, however as the number of possible isomers grows, the capability of fitting a photoionization spectrum to quantitatively distinguish the various combinations of isomers decreases. Furthermore, to obtain high resolution photoionization spectra, it is necessary to acquire a large number of experiments for averaging at each photon energy, properly accounting for changes in photon flux at each energy level. The absolute number of experiments required is dependent on the concentrations and absorption cross-sections of target species.

An alternate technique that has many of the features of VUV-PIMS and some advantages is synchrotron-based photoelectron photoion coincidence (PEPICO) spectroscopy. This powerful method yields not only mass spectra but also the corresponding photoelectron spectra (PES), which, relative to the photoionization spectrum, can be thought of as a higher resolution fingerprint of molecular structure. Like photoionization spectra, the photoelectron spectra can be used to identify discrete species in mixtures of isomers. However, the sharper and richer set of features in the photoelectron spectrum allows more complex mixtures to be discretized. Although the potential for isomer differentiation was established early in the development of PES [30], the expansion of imaging coincidence techniques has been recently exploited by the combustion community to answer the need for an *in-situ*, real-resolved, universal probe of complex gas-phase chemistry [31–36]. The same detection schemes are also applied in other fields including atmospheric chemistry [37–39] and catalysis [40,41].

The rich information content from PEPICO is very attractive, but coincidence schemes need a very low ratio of ionization events per photons pulse to work (<0.01), and therefore are mostly used with continuous synchrotron sources or high repetition lasers ($\geq$100 kHz). PEPICO experiments are also normally performed with steady state or pseudo-steady state reactors, such as flow tubes and flames. HRRSTs were specifically developed for coupling with synchrotron-based detectors and following HRRST/VUV-PIMS experiments, coupling an HRRST to a PEPICO detector is a logical step. The advantages of shock tubes for high temperature kinetics studies are well-established as are the benefits of PEPICO for determining the composition of complex mixtures of open and closed shell species. The HRRST/PEPICO method is expected be an excellent complement to other more established techniques and a focus of future work will be a rigorous comparison of the benefits of various methods and the potential for synergistic studies.

The HRRST/PEPICO combination presents a number of significant challenges. First, although the HRRST repetition rate (1 Hz in this work) is very high for a shock tube, it is a low repetition rate pulsed source. Still, this rate is not dissimilar to pulsed photolysis sources (4–10 Hz) used with other experiments that employ VUV-PIMS [19]. This rate results in an effectively low duty cycle for the PEPICO instrument. The low duty cycle cannot be compensated for by simply increasing the photon flux, though, as a low flux rate is necessary to prevent so-called false coincidences becoming overwhelmingly frequent, reducing the S/N. Second, the gas composition in a shock tube changes rapidly and dramatically during an experiment, and thus it is necessary to conduct time resolved experiments. Finally, the pressure changes in a shock tube experiment are large, and these induce pressure changes in the spectrometer chamber must be considered. The last two challenges are common to HRRST/TOF-MS experiments, and have been either surmounted or are the focus of ongoing work [21–23]. In the following sections, we describe a new HRRST built at Institut de Combustion Aérothermique Réactivité Environnement - Center National De La Recherche Scientifique that has been designed to exploit the strengths of synchrotron photoelectron photoion coincidence (PEPICO) spectroscopy at the DESIRS beamline at the SOLEIL synchrotron facility [42].

First, the ICARE-HRRST is described, and its suitability for the demanding task of producing thousands of repeatable shocks, needed to obtain a sufficient signal-to-noise ratio via the coincidence scheme is demonstrated. We then present results from the first shock tube/PEPICO experiments, during which pyrolysis of ethanol was studied (1232–1525 K, ~7 bar) in non-sooting and sooting conditions. The experiments were conducted on the SAPHIRS end-station [43] of the DESIRS beamline [42] at the SOLEIL synchrotron facility with the DELICIOUS III double imaging (I^2PEPICO) spectrometer [43,44]. Ethanol was selected for these initial experiments because there is a rich literature of experimental [45–50] and theoretical [48,51–53] research that could guide design of experiments and interpretation of the results. Furthermore, ethanol pyrolysis spans regimes from non-sooting conditions where products are dominated by small hydrocarbons to sooting

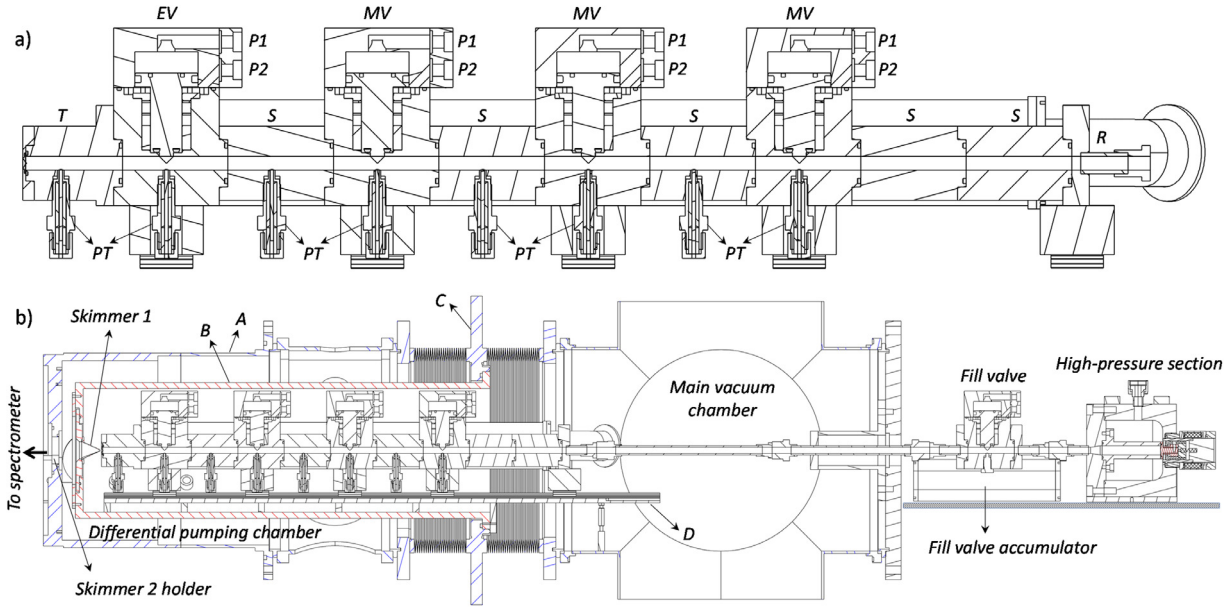

Fig. 1. a) Cross-sectional view of the part of the driven section of the ICARE-HRRST that sits inside the SAPHIRS vacuum chamber at SOLEIL. The part that connects *R* to the vacuum feedthrough is a section of tube and is not shown. *EV*: end valve; *MV*: middle valves; *T*: end section; *S*: spacers; *R*: connection element; *PT*: pressure transducer holders. Compressed air is connected to ports *P1* and *P2*. b) ICARE-HRRST coupled with DESIRS-SAPHIRS. *A*: DESIRS-SAPHIRS outer chamber; *B*: DESIRS-SAPHIRS inner chamber; *C*: movable support flange for chamber B; *D*: slab with linear guides.

conditions where polyaromatic hydrocarbons are formed in large amounts. These different regimes are easily accessed by changing reaction temperatures. These two distinct regimes permitted different aspects of the HRRST/PEPICO combination to be tested. The goal of the present investigation was not to provide a detailed analysis of the kinetics or mechanism of ethanol pyrolysis, but to examine the experimental capabilities of the unique HRRST/i^{2}PEPICO combination. These first experiments with the ICARE-HRRST/PEPICO apparatus represent a demonstration of the potential of the methodology. During the current studies, a number of areas for improvements were identified, and these are also discussed.

2. Experimental section

In this section, the design of the ICARE-HRRST and its integration into the DESIRS beamline is presented. In addition to the shock tube, the data acquisition process and automation of the entire facility are also briefly discussed. The performance of the ICARE-HRRST is demonstrated with the results from laboratory-based experiments prior to installation of the shock tube at the beamline.

2.1. ICARE-HRRST

The ICARE-HRRST is intended for use as a standalone lab instrument as well as at synchrotrons. The design is based on a similar apparatus reported by Tranter and Lynch [17] (ANL-HRRST). However, a number of significant changes have been made that were necessary to allow insertion of the ICARE-HRRST into the constrained space in the SAPHIRS chamber at DESIRS (Fig. 1b). The main features of the ICARE-HRRST are described below, and a detailed description and drawings are available in the Supplementary Material. Figures labelled "Fig. SXX" refer to figures in the supplementary file.

The driver section of the ICARE-HRRST consists of a high-pressure chamber and a fast acting, high-pressure, solenoid actuated valve (Fig. 2). The high-pressure chamber is a cylinder of 304 stainless steel and has a 78 mm i.d. and volume of 0.334 L. The chamber is rated for pressures up to 100 bar. The driven section extends into the high-pressure chamber. This part of the driven section has an i.d. of 12 mm which is reduced through a converging nozzle to match the rest of the driven section (8 mm). The reduction in cross-sectional area, a factor of 2.25, results in higher shock Mach numbers compared to a straight tube for the same initial ratio of driver pressure (P_4) to driven section pressure (P_1) [54]. The driver valve is opened by an overdriven solenoid and closed by a spring. The valve is similar to that described by Tranter and Sikes [55], more details have been provided in the supplementary material. The final part of the driver section is an accumulator tank (2.2 L) that is necessary to maintain a consistent P_4 during high-repetition-rate operations. P_4 is monitored by a Honeywell LM-BP211DL sensor.

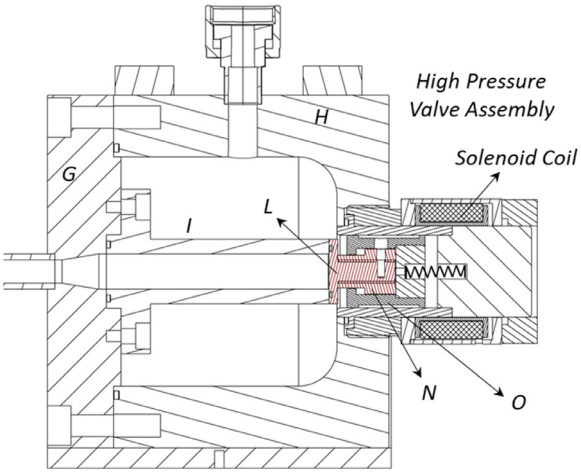

Fig. 2. Cross-sectional view of the driver section showing the high-pressure chamber and solenoid actuated valve. *G*: flange with convergent section; *H:* main chamber body; *I*: leading part of the driven section; *L*: poppet; *N*: outer body; *O*: armature body. Parts *L*, *N* and *O* form the armature.

The driven section of the ICARE-HRRST was designed in a modular fashion, Fig. 1a, that allows it to be easily reconfigured with a length changed to meet specific needs. The driven section has a bore of 8 mm, slightly larger than in the original ANL-HRRST (6.35 mm) but smaller than the 12.7 mm bore miniature shock tube constructed by Lynch at the University of Illinois at Chicago (UIC-HRRST) [56] and the 15 mm bore shock tube designed by Matsugi [57]. The larger bore results in longer test times (~800 μs) than are achievable in the ANL-HRRST (~ 300 μs [21]). The driven section modules consist of spacer sections (S) and pneumatically actuated valves (*EV, MV* and *FV*). The sections are 60.0 mm in length and connected by a boss and socket arrangement that precisely aligns the bores. Viton O-rings provide seals between the sections and tie rods hold the parts together. Pressure transducers, *PT*, (CHIMIE METAL A25L05B, 2 mm diameter) are located in the base of the valves and spacer sections in removable holders. The *PT*s are spaced 60.0 mm on center. The final pressure transducer is 20.0 mm from the end wall and the shock velocity at the end wall is obtained by extrapolation.

The valves *EV* and *MV* are used to exhaust gases from the shock tube and *FV* admits fresh reagent mixture to the driven section, detailed descriptions of their functions, design and timing are given in the supplementary material. The driven section ends with the terminal section, of which there are currently two. The first is designed to hold nozzles (100–400 μm orifice diameters) that form the first part of the interface to the ionization chamber where the DELICIOUS III spectrometer is mounted. In the second, the nozzle is replaced by a PCB pressure transducer (113B24 covered by a thin layer of RTV) allowing laboratory-based tests to characterize the pressure time-histories behind reflected shock waves. Due to the small bore of the ICARE-HRRST, it is not possible to simultaneously mount a sampling nozzle and endwall pressure transducer in the terminal section.

The design of the pneumatic valves is similar to that in reference 17. However, to maximize conductance through the valves, they have been constructed with two ports on opposite sides rather than just one as in ref [17]. On the *EV* and *MV* valves the ports are connected to exhaust manifolds whereas on the *FV* valve they are connected to reservoirs of reagent mixture. More details are presented in the supplementary information. The exhaust manifolds are continuously evacuated by a roots blower pump (3900 m^3 / hr; Edwards-EH500 / GV-80) through KF-40 fittings, flexible hoses, and vacuum feedthroughs. The reagent reservoirs attached to *FV* are equipped with pressure relief valves, and one also has a MKS 722B capacitance manometer to measure the loading pressure in the driven section, P_1. The reagent reservoirs are continuously filled from an automated mixture preparation system, Section 2.3. Compressed air for operating the pneumatic valves is supplied via double acting solenoid actuated valves (Parker-Viking Xtreme P2LCX series). *FV* and *EV* are connected to individual control valves while the three *MV*s are all connected to a single control valve. Thus, the five pneumatic valves are operated as three discrete units. Two thermocouples are attached to the end section and *EV* to monitor the driven section temperature, T_1. Under vacuum in the SAPHIRS chamber the *EV* temperature needs also to be monitored to avoid excessive heating up during high repetition operations.

2.2. Data acquisition and electronics

Operation of the ICARE-HRRST is fully automated through a LabVIEW program and purpose-built electronics similar to those used in Ref. [17]. The methodology and timing strategy were similar to those employed with the ANL-HRRST and UIC-HRRST. The program generates digital control signals via a multifunction DAQ card (National Instruments PCIe-6361) and monitors various analog signals via the same card. For every shock, all the state information (e.g. P_1, P_4, T_1, nominal mixture composition, and the signals from the CHIMIE METAL sensors) necessary to recalculate shock properties are recorded along with ancillary information. In addition, the time dependent spectral information from the i^2PEPICO instrument was recorded for every shock. Consequently, the data can be post-processed to include or exclude individual experiments and to bin experiments based on desired ranges of reflected temperature (T_5) and pressure (P_5). The synchronization between DELICIOUS-III and the shock tube was performed with a NIM signal from a Stanford DG535 delay pulse generator that was fed into the Time to Digital Converter (TDC) managing the data acquisition of the DELICIOUS III spectrometer [44]. The TDC continuously measures the arrival of the charged particles to the position sensitive detectors with a 120 psec step and yields time and position information [44,58]. The arrival of photoelectrons is measured with respect to the shock wave timing signal and thus contains the kinetic data because the electron time-of-flight, on the order of a nsec, is independent of its initial kinetic energy and is negligible with respect to the kinetics timescale. The ion TOF is measured with respect to the electron arrival and carries the *m/z* information. The ionization events that build up the photoelectron image from which the PES is extracted are tagged by the ion mass, reaction time and experiment number. The start of data acquisition was delayed relative to firing the shock tube, and 8 ms of data were obtained that spanned the pre-shock and post-shock regions. For several thousand experiments, at the end of the experimental campaign, the repetition rate was increased from 1 Hz to 1.5 Hz with no degradation of the performance of the shock tube or the i^2PEPICO instrumentation.

To obtain the time intervals for passage of the incident shock wave between consecutive CHIMIE METAL sensors, a different approach has been taken compared to Ref. [17]. Here the pressure profiles from each sensor are digitized (25 MS/s, GAGE-Applied Octopus 14-bit PCIE card) and stored. For each channel, the incident shock is located with a LabVIEW program, permitting the time interval and hence shock velocity to be obtained. The code is sufficiently efficient to calculate velocities and post-shock conditions (P_2, T_2, P_5 and T_5) on-the-fly allowing performance of the ICARE-HRRST to be monitored as it runs.

2.3. Reagent mixture preparation

The high-repetition-rate of the HRRST requires reagent mixture to be supplied almost continuously to the driven section. For this purpose, a separate mixing apparatus was built. This is comprised of a bubbler for entraining vapor from liquid fuels into a carrier gas (here argon) and a mixing station with three MKS mass flow controllers (MFC, model 1179A) and a six-liter reservoir to store the mixture. One MFC regulates the flow at the exit of the bubbler, while the second one was used to add additional argon to achieve the desired mixture compositions. Solenoid valves were placed at the exit of each MFC to start and stop the flow. Downstream of the solenoid valves, the gas streams enter a manifold with a static mixing element. Operation of the mixing rig is fully automated through a LabVIEW program and control electronics. The pressure in the reservoir is monitored and maintained in a certain range by adding fresh reagent mixtures needed. Over the course of one thousand shocks, the reservoir will be topped up several times. The reservoir outlet is connected to the fill-valve accumulators through a vacuum regulator that is used for maintaining the pressure P_1 at a desired value. In general, the initial ten experiments in a batch of shocks are discarded while P_1 and P_4 values reach stable values. In these experiments, ethanol was purchased from Sigma Aldrich (>99.8% pure) while argon was supplied by Air Liquide (>99.9999% pure).

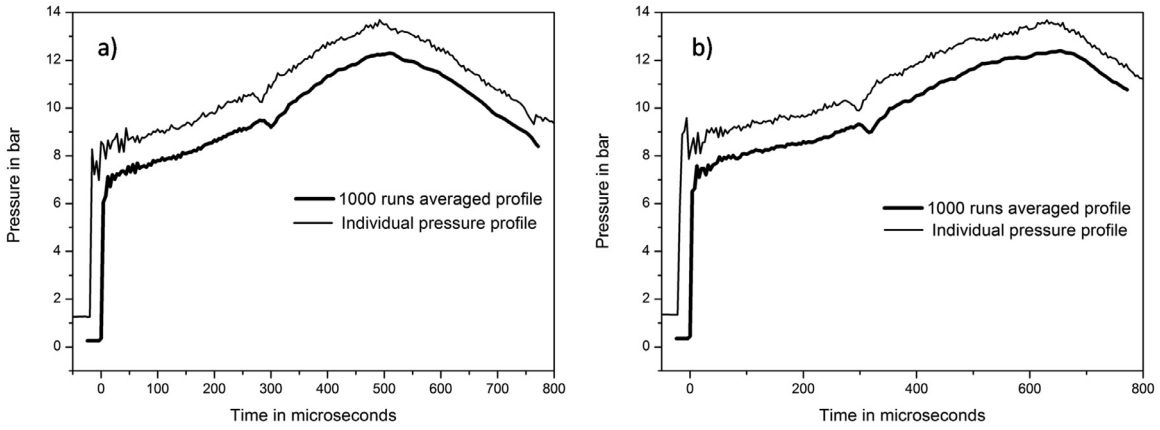

Fig. 3. Pressure time-histories for a single experiment and an average pressure over 1000 experiments for the following conditions: a) T_5 = 1509 K, P_5 = 7.3 bar; b) T_5 = 1297 K, P_5 = 7.8 bar. For clarity, the individual pressure profiles are offset relative to the averaged profile (+1 bar, -20 μs). Without the offset, the profiles would be largely indistinguishable.

2.4. The DESIRS beamline and coupling of the ICARE-HRRST and DELICIOUS-III

The experiments were conducted at the monochromatic branch A of the undulator-based DESIRS beamline [42]. At DESIRS, an argon gas filter eliminated higher order photons prior to the monochromator, in which a 200 g/mm low dispersion grating was chosen to deliver photon resolutions of around 25 meV, over the 10–11 eV photon energy range used in this work. Branch A terminates with the SAPHIRS molecular beam chamber [43] which is equipped with DELICIOUS-III, the i^{2}PEPICO spectrometer [44]. DELICIOUS III consists of a velocity map imaging (VMI) spectrometer and a modified Wiley–McLaren time-of-flight (TOF) imaging spectrometer that simultaneously detects electrons and ions, respectively. The 3D ion momentum distribution is obtained from the ion TOF referenced to the arrival time of the corresponding electron and its location on the position-sensitive detector. A second position-sensitive detector is used to collect electron images on the VMI. These images can be treated with an Abel inversion algorithm [59] to obtain photoelectron spectra. The coincidence scheme is applied to filter the photoelectron images by ion momentum prior to Abel inversion. In the present work, the scheme is used to mass select the photoelectron spectra, and to consider only events correlated to molecules coming from the shock tube, i.e. to ions having a net velocity along the direction of the molecular beam transporting molecules from the shock tube to the spectrometer interaction (ionization) region.

The ICARE-HRRST is coupled to DELICIOUS III by a double differentially pumped molecular beam sampling interface. Fig. 1 shows a schematic of the ICARE-HRRST mounted in the SAPHIRS chamber, the fill valve and high-pressure section are outside the chamber. The driven section of the shock tube terminates with a nozzle that is aligned with a skimmer forming the first of the two stages of differential pumping. The double differential pumping in combination with careful selection of nozzle and skimmer orifice sizes and the distance between them is necessary to maintain safe operating pressures in the spectrometer chamber ($< 1 \times 10^{-6}$ mbar) while obtaining adequate signal levels. Gases eluting from the shock tube form a supersonic jet freezing the gas composition. The core of this jet passes through the first skimmer forming a molecular beam. A second skimmer is mounted on the left most wall of Fig. 1, the entrance to the spectrometer chamber, and the core of the molecular beam passes through the second skimmer into the ionization zone of the spectrometer. Careful alignment of the nozzle and two skimmers is essential to maximize signal. The position of skimmer 2, Fig. 1, is fixed and centered on the ion source of the spectrometer. Skimmer 1, however, can be moved under vacuum in the *X*, *Y* and *Z* axes by precision motor driven screws, see [43,44]. By introducing a small flow of argon into the chamber, the two skimmers can be precisely aligned and moved to a desired separation by monitoring the spectrometer signal. Unfortunately, due to the weight of the ICARE-HRRST and the need to have the fill valve and high-pressure section outside the vacuum chamber this alignment cannot be done with the shock tube installed. To ensure chamber *B*, Fig. 1, did not move after aligning the skimmers a new chamber was made with six support feet near the skimmer end that are positioned after aligning the skimmers. Measurements of signal intensity with and without the shock tube installed confirmed that alignment was kept. During the initial sets of experiments, conservative choices for the diameter of the first skimmer and the separation between the nozzle and first skimmer, and first and second skimmers were made. While these reduced signal levels, they did allow safe operation while experience was gained with the system. In the latter experiments, more optimal orifice sizes and separations were selected. Details of the configurations of the nozzles and skimmers are given in later sections.

2.5. ICARE-HRRST performance

Prior to experiments at SOLEIL, the performance of the ICARE-HRRST was assessed in the laboratory to determine the reproducibility of shock waves and the operating characteristics of the instrument. The tests were performed with helium as the driver gas and argon as the driven gas and P_5-time histories were recorded for two nominal conditions: 7.8 bar and 1297 K, and 7.3 bar and 1509 K. One thousand experiments were performed at each condition. Examples of pressure/time histories averaged over 1000 shocks and a single shock are shown in Fig. 3 for both experimental conditions. As expected, the observation time, limited by the arrival of the rarefaction waves and the subsequent drop in the pressure and temperature, is shorter for higher temperatures, 500 μs at 1509 K compared to 700 μs at 1297 K. Similar to the ANL-HRRST and UIC-HRRST, P_5 changes during the observation period due to boundary layer growth. In Fig. 3, the increase in P_5 is quite large going from about 8 bar to about 12 bar. Of course, the change in P_5 would need to be taken into consideration for making quantitative measurements but is not an impediment to the current work. As the pressure profiles are very reproducible for a given range of T_5 and P_5 it should be possible to use profiles measured in the lab to analyze future datasets from PEPICO experiments where the profiles cannot be obtained.

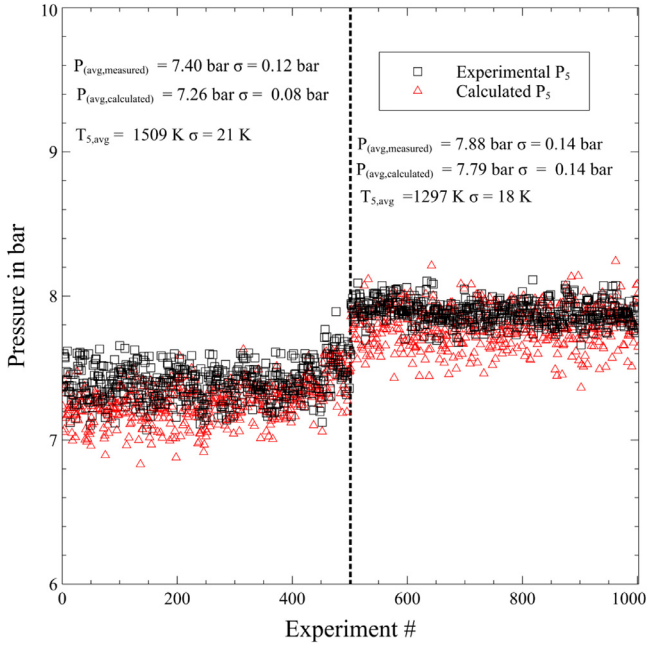

Fig. 4. Distribution of measured and calculated reflected shock pressures using extrapolated velocities to the end-wall of the shock tube.

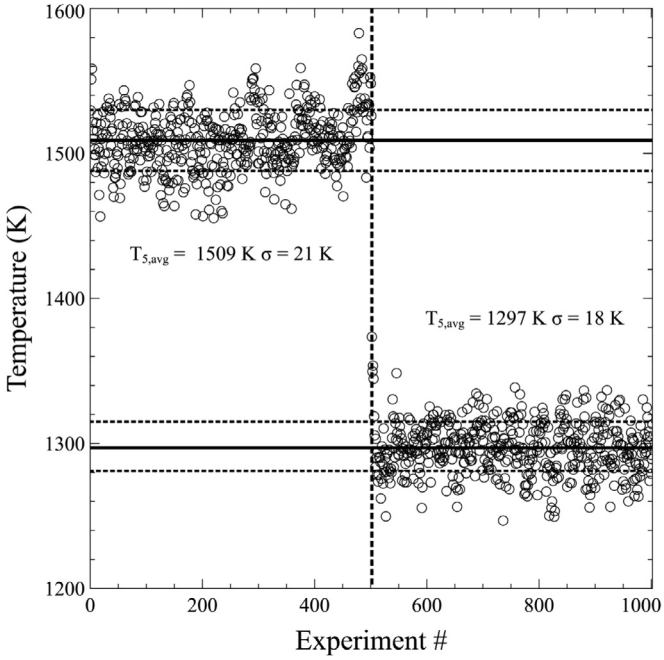

Fig. 5. Distribution of calculated reflected shock temperatures using extrapolated velocities to the end-wall.

For each shock that forms the averaged signals in Fig. 3, the measured P_5 was obtained from the first 40 μs following formation of the reflected shock wave. P_5 was also calculated by extrapolating the shock wave velocities to the end-wall based on the last five pressure sensors signals and subsequently solving the conservation equations. There is excellent agreement, in Fig. 4, between the measured pressures and the pressures calculated using the extrapolated velocities. The average pressure and temperature conditions for the first set of data are 7.8 bar and 1297 K with standard deviations of 0.1 bar and 18 K, respectively, and for the second set of data 7.3 bar and 1509 K with standard deviations of 0.1 bar and 21 K. In Fig. 5, the distributions of calculated T_5 based on the extrapolated velocity are reported. The variation in the P_5 and T_5 can be attributed predominantly to variation of P_1 and P_4. In particular, the variation in P_1 is due to slight shifts in the filling reservoir pressure. P_5 follows a similar trend and variation to P_1.

3. HRRST/I^{2}PEPICO experiments on ethanol pyrolysis

The first ever shock tube / I^{2}PEPICO experiments were conducted on ethanol pyrolysis. At high temperatures, the thermal decomposition of ethanol proceeds mainly through three channels [47–49,52]:

$$C_2H_5OH = C_2H_4 + H_2O \quad (R1)$$

$$= CH_3{+}CH_2OH \quad (R2)$$

$$= C_2H_5{+} OH \quad (R3)$$

Reaction channels R1 and R2 are identified as major unimolecular pathways in the decomposition of ethanol for a wide range of temperatures and pressures [46,47,49] and some of the products should be directly observable in these experiments. It is unlikely that CH_2OH and C_2H_5 would be detectable as the rates of their unimolecular dissociation ($> 10^7$ s^{-1}) are very high at the reaction conditions studied. Similarly, the OH radical is rapidly consumed in bimolecular reactions and will reach only a very low concentration.

The present work spans T_5 of 1232–1571 K, and P_5 from 6.2–7.5 bar. Two photoionization energies were chosen, 10.0 eV and 11.0 eV. Experiments at 11.0 eV allowed C_1-C_6 hydrocarbons including the fuel molecule to be monitored (ethanol has an ionization energy of 10.41±0.05 eV [60]). However, the signals from ethanol and other major species were sufficiently intense at 11.0 eV that sensitivity to minor species was reduced. This sensitivity reduction was primarily from increased background caused by false coincidences from photoions of the major species. The 10.0 eV experiments avoided this issue, as the photon energy was below the ionization energy of ethanol and ethylene, which resulted in enhanced detection of trace species including polycyclic aromatic hydrocarbons, at the expense of no longer being able to simultaneously monitor ethanol. In addition to varying the reaction conditions and ionization energies, the concentration of ethanol was also adjusted. In initial experiments, a relatively high concentration was used to ensure adequate signals. In subsequent experiments, much more dilute mixtures were used, and signal levels were maintained by improvements to the molecular beam sampling. The high concentration experiments are discussed first.

3.1. Experiments with high ethanol mole fractions (0.027)

The experiments presented in this section were conducted with mixtures containing 2.7% ethanol in argon. The first element of the molecular beam sampling system was an electroformed nickel nozzle (Servometer) terminating the driven section. Two nozzles were alternatively used and had orifices of 0.35 mm and 0.4 mm. The two skimmers completing the MBS were Beam Dynamics Model-2. The first stage skimmer (Skimmer 1, Fig. 1), had an orifice of 0.5 mm, whereas the second stage skimmer at the spectrometer entrance (Skimmer 2 position indicated in Fig. 1), had a 2.0 mm orifice. The distance between the nozzle tip and the skimmer tip in chamber *B* was set at 3.2 mm. This is close to the distance where maximum quenching in the supersonic jet is attained [61]. With this combination of nozzles and skimmers, the pressure inside the various chambers could be maintained at acceptable levels (dynamic pressure of 10^{-4}–10^{-3} mbar in the main chamber and

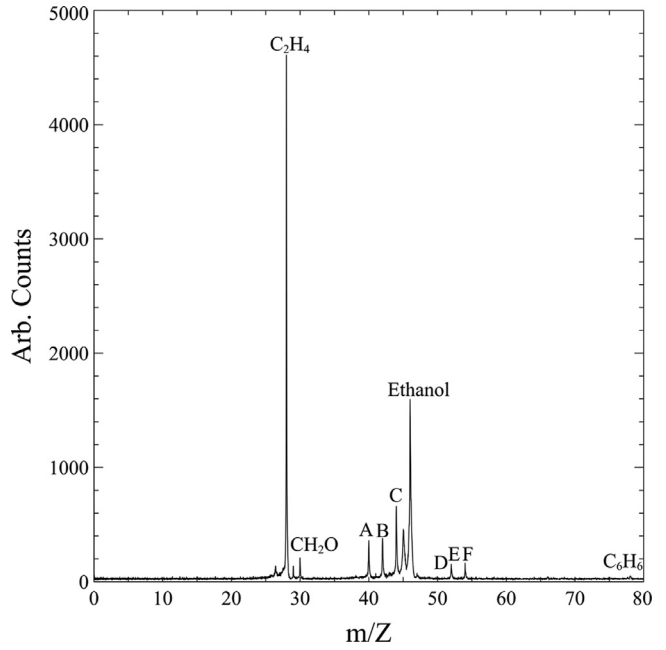

Fig. 6. Mass spectrum obtained for $T_{5,mean}$ = 1232 K, $P_{5,mean}$ = 7.4 bar, 2.7% ethanol in argon. A: propyne, B: propene/ketene, C: acetaldehyde+ vinyl alcohol, D: vinylacetylene, E: 1,3 butadiene (possible contribution from 1-butyne). Photon energy 11.0 eV.

10^{-8}–10^{-6} mbar in the spectrometer chamber) with turbomolecular pumping (2000 l/s Adixen ATP3000M and 1000 l/s Seiko Seiki STPH1000C for the main chamber, three turbo-molecular pumps (300 l/s, Edwards nEXT300D) for the differential chamber, and two turbo-molecular pumps (1000 l/s, Leybold TurboVac1000) for the ionization chamber). The experimental results are given in Figures 6–8, 11–16 and are categorized into four cases based on the T_5 and P_5 ranges of the experiments, as well as the photon energy and the fuel concentrations. The specific conditions for each case are given in the following sections.

3.1.1. Low temperature, 11.0 eV photon energy

The first set of ethanol pyrolysis experiments were carried out at a photon energy of 11.0 eV. The set consisted of 15,000 experiments, $T_{5,mean}$ = 1232 K, σ = 19 K and $P_{5,mean}$ = 7.4 bar, σ = 0.2 bar ($P_{5,mean}$ / $P_{1,mean}$ ~ 25). Figs. 6 and 7 show examples of the experimental results which were obtained from averaging the 15,000 experiments. The mass spectrum obtained from integrating over 1.25 ms of pre-shock and 6.55 ms of post-shock measurements is presented in Fig. 6. This mass spectrum contains contributions from molecules eluting from the shock tube before the reflected shock wave is formed (i.e. the pre-shock region), species from behind the reflected shock wave (i.e. post-shock region) and species from after the arrival of the rarefaction waves (at around 700 µs based on Fig. 3). Thus, the relative values of the peak heights may be weighted towards the products which are present in the mixture after quenching. Despite this, mass spectra such as these are useful for obtaining an overview of product distributions and identifying species of interest for which spectra can be obtained from appropriate parts of the whole dataset e.g. the first couple of hundred microseconds of reaction. The process of obtaining results from limited temporal regions is described later.

For each mass, the photoelectron image can be extracted from the underlying dataset [43]. An example 2D of photoelectron image after Abel inversion for m/z 28 is shown in Fig. 7a. The photoelectron spectrum can be obtained from the 2D photoelectron image. In the present work, the S/N is sufficiently large to obtain well-defined VMI-photoelectron spectra for a number of the smaller species, for example ethylene (mass:charge ratio, m/z 28, Fig. 7b). Similarly, it was possible to identify other products including formaldehyde (CH_2O, m/z 30), propyne (m/z 40), acetaldehyde+ vinyl alcohol (CH_3CHO and CH_2CHOH, m/z 44) and vinylacetylene (m/z 52). The photoelectron spectra and comparisons to literature spectra are available in the supplementary material. While most of these species could easily be identified based on m/z and ionization energy, the results demonstrate that reliable PES can be obtained from the HRRST/PEPICO experiments.

Considering m/z 52, there are several isomers of C_4H_4 that could contribute to this peak, but the photoelectron spectrum reveals that the largest contribution to the observed peak is from vinylacetylene (Fig. 8). In this case, the experimental peaks are quite broad, due to the fact that the signal for m/z 52 is relatively low. Indeed, although the photoelectron VMI spectrometer is capable of absolute electron resolutions in the 30–70 meV range for the moderate extraction field used in this work, the original images have to be binned to increase the S/N per pixel for the Abel inversion to work, leading to decreased resolution. Thus, not all the features of the vinylacetylene PES are observed. However, the good match between the binding energies at the experimental maxima and the peak energies in the vinylacetylene PES confirms that the small m/z 52 peak in Fig. 6 corresponds to vinylacetylene. The absence of peaks at around 8.25 eV also rules out the possibility of a contribution from cyclobutadiene, while the small shoulder at around 9.2 eV could be due to a small contribution from 1,2,3-butatriene. The PES presented in Fig. 8 is adequate although of relatively low resolution. However, in Section 3.2 we show that it can be considerably improved by changing the photon energy and increasing the number of averaged signals.

At m/z 54 a large peak is observed that corresponds to features in the literature PES for 1,3-butadiene [32]. However, unlike the analysis of m/z 52 where some isomeric species could be excluded based on the 11.0 eV PES, we cannot exclude 1-butyne as being a contributor to the experimental m/z 54 PES at 11.0 eV (Fig. S10). For several other species, the signal intensity is too low to obtain well-defined PES indicating that either more experiments would be required or that S/N should be improved by other means.

In a prior shock tube study, Kiecherer et al [46] used TOF/MS with electron impact ionization to study ethanol pyrolysis, T_5 = 1300–1510 K and P_5 = 1.1 bar. They identified a peak corresponding to m/z 44 and hypothesized, based on modeling that it corresponded to acetaldehyde and not vinyl alcohol (CH_2CHOH). The present results clearly confirm, at similar T_5, acetaldehyde is formed as one of the main primary products of ethanol decomposition. Later in the text, we also show that vinyl alcohol is formed in lower concentrations. The ability to distinguish isomers, even when one is minor relative to the others, is a powerful feature of the HRRST/PEPICO method.

The final peak analyzed in this initial dataset was m/z 42. Identification of the species contributing to m/z 42 was quite challenging. The photoelectron spectra for ketene (m/z 42.08) and propene (m/z 42.04) are nearly identical (Fig. S9) and the experimental PES lacks sufficient resolution to distinguish between the two compounds. Obtaining a sufficiently well-defined experimental PES to distinguish ketene from propene with the HRRST/PEPICO experiment would require much better resolution. This could potentially be obtained either by lowering the extraction field or using threshold photoelectron techniques where the resolution can be <1 meV [66]. However, these methods would require a much longer acquisition time due to the necessary photon energy scanning (see for instance reference 32). Either of the methods would be challenging in terms of acquisition time and source stability, and the low duty cycle of the shock tube relative to pseudo-steady state reactors.

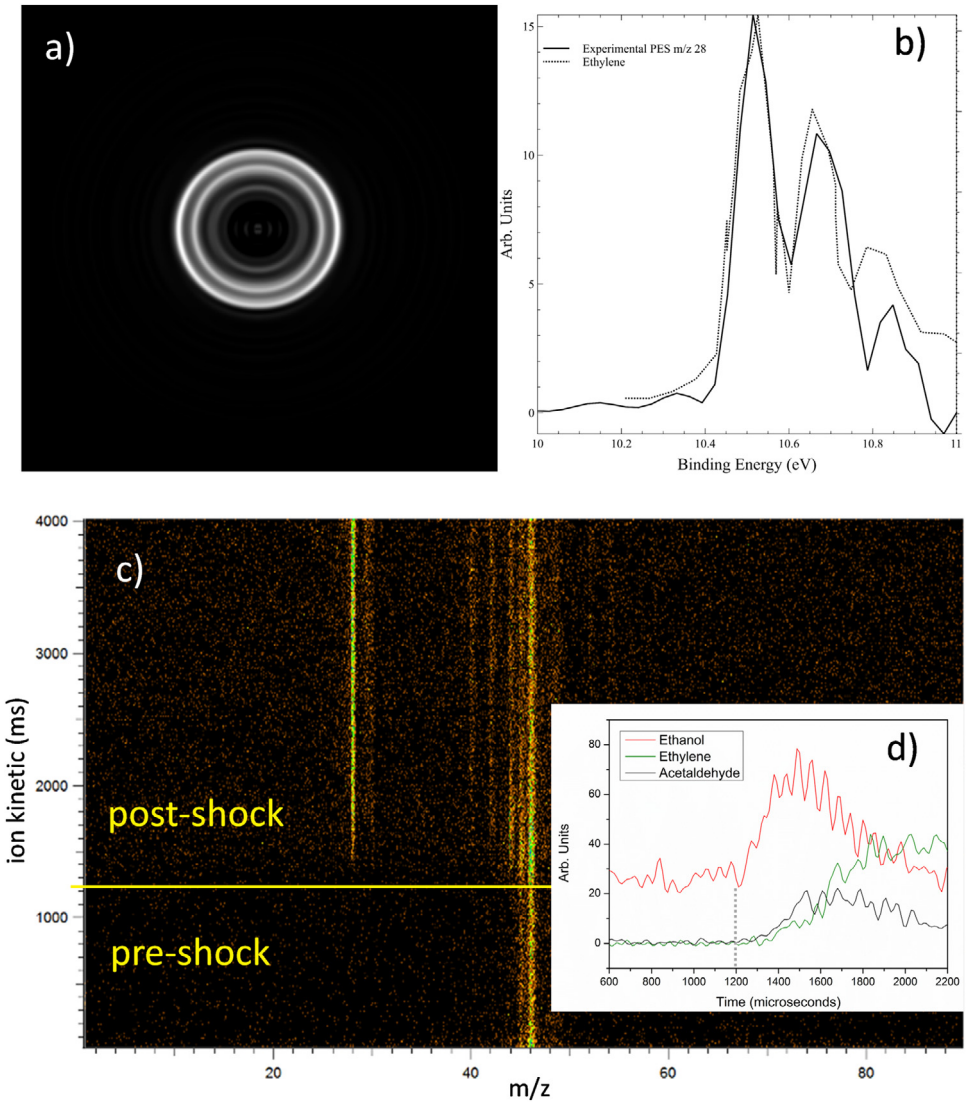

Fig. 7. a) Photoelectron image corresponding to m/z 28; b) comparison of photoelectron spectra for m/z 28 (experimental) and ethylene [62]; c) ion kinetics for each mass, horizontal line distinguishes the pre-shock and post shock region; d) temporal profiles of ethanol (red), ethylene (green), and acetaldehyde (black), with a vertical line distinguishing pre-shock and post-shock area. The experimental profiles were obtained by taking vertical slices from Fig. 7c.

In addition to the mass spectrum and photoelectron spectra, the temporal histories of ions were also obtained. The raw data can be reduced in many ways and one particularly useful method for this work is to obtain plots such as shown in Fig. 7c. In this figure, the number counts of the different ions are plotted on two axes which reference their arrival times at the detector relative to the trigger (time zero). The X-axis represents m/z, of an ion, while the Y-axis represents the arrival time relative to time zero. Thus, a horizontal slice of the image gives a mass spectrum at a specific time relative to the trigger (e.g. Fig. 6), while a vertical slice yields the time history for a specific m/z. Examples of time histories of discrete masses obtained by taking vertical slices from the ion kinetics graph are presented in Fig. 7d. Fig. 7c contains data before and after shock wave reflection at the endwall, the time marked by a horizontal line at 1.25 ms. Before 1.25 ms, essentially the only species observed are the parent ion of ethanol (m/z 46) and $C_2H_5O^+$ (m/z 45) from dissociative ionization of the ethanol cation. The observation of mass 45 in the pre-shock region is consistent with its appearance energy of 10.8 eV [67]. At 1.25 ms in Fig. 7c, other ions also begin to appear, indicating products being formed. The formation of the reflected shock is most easily determined from integrated mass peaks for primary products vs. time plots. An example of this is shown in Fig. 7d where time histories of the peaks for acetaldehyde and ethylene are shown along with ethanol.

In principle, the plots shown in Fig. 7d are equivalent to concentration/time plots from which kinetic parameters could be derived. However, the species temporal profiles are influenced by pressure changes inside the mass spectrometer chamber that are induced by the rapid and large pressure changes in the shock tube during an experimental cycle. This problem is well-understood and entirely the same as encountered in shock tube/ TOF-MS experiments [68,69]. In those experiments, an inert internal standard is added to the reagent mixture and used to correct for pressure changes in the spectrometer chamber [68,69]. This method is easy to implement with electron ionization but more challenging with photoionization [23]. However, once an internal standard has been developed, it will be used in future experiments to obtain accurate species temporal curves and permit accurate concentrations of species to be measured. With respect to the current work, it is possible to obtain relative concentrations of ions from which branching ratios can be estimated in a similar manner to that used with

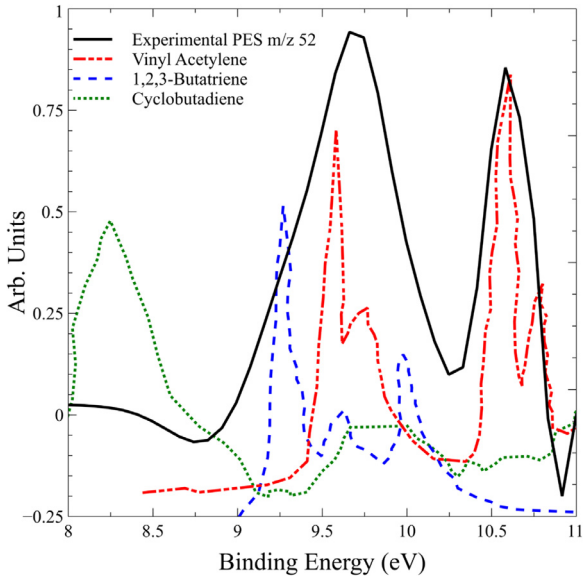

Fig. 8. Photoelectron spectra for m/z 52 (experimental), vinylacetylene [63], 1,2,3-butatriene [64], and cyclobutadiene [65]. Photon energy equal to 11.0 eV.

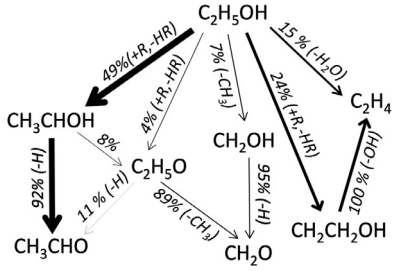

Fig. 9. Integrated rates of production, 2.7% C_2H_5OH in argon, T_0 = 1232 K, P_0 = 7.4 bar. The percentages refer to the consumption of the reactant species, the arrow thickness is proportional to the corresponding flux. CRECK model [70].

HRRST/VUV-PIMS [22,23] considering that ions from similar reaction times experience the same pressures in the molecular beam. Thus, various competing pathways can be assessed and compared with modelling results.

Chemical kinetic modelling of ethanol pyrolysis was performed with the CRECK model [70] using the homogenous reactor model of COSILAB [71]. The reaction conditions were set at T_0 = 1232 K, P_0 = 7.4 bar, and the constrained pressure profile was implemented using the pressure history from Fig. 3b. The integrated rates of production over the first 700 µs for the main reaction pathways are presented in Fig. 9. Around 15% of the fuel decomposition proceeds through reaction 1 which leads directly to the formation of ethylene, while the pathway to formaldehyde through reaction 2 accounts for 7% of the fuel decay. The remaining fuel decomposition pathways involve H-radical abstraction by H, OH, and CH_3. In particular, the H-abstraction reactions leading to formation of CH_3CHOH account for 49% of the fuel depletion. Once formed, CH_3CHOH mostly decomposes to acetaldehyde + H. Another pathway to acetaldehyde involves the formation of C_2H_5O, which in turn comes from the fuel molecule through H-abstraction (4% of the fuel consumption) or from the isomerization of CH_3CHOH, but this pathway is only minor since C_2H_5O mainly decomposes to formaldehyde + CH_3. Finally, the formation of the CH_2CH_2OH radical (24% of the fuel consumption) leads ultimately to ethylene and OH radical. The C3 and C4 products observed in Fig. 6 derive from the reactions between C2 intermediates and CH_3 or other C2 intermediates, respectively.

The temporal profiles for the three main products, formaldehyde, ethylene, and acetaldehyde, are presented in Fig. 10a together with the experimental profiles over 700 µs after the shock wave reflection at the end-wall for the corresponding m/z values (Fig. 10b, filtered raw data). There is excellent qualitative agreement between the simulations and the experiments. A fast rise in the acetaldehyde concentrations (m/z 44) can be observed at early times before reaching a maximum at around 400 µs while the ethylene profile (m/z 28) is characterized by a slower but monotonic rise. At later times, the concentration of ethylene is much larger than that of acetaldehyde, while formaldehyde (m/z 30) is formed in relatively small amounts. It is important to underline that the profile for m/z 44 (Fig. 10b) contains two contributions from acetaldehyde and vinyl alcohol (see Fig. S10 for the PES curve), acetaldehyde being the major product. Vinyl alcohol may be formed by H-scission from the terminal and central carbon atoms of the CH_3CHOH and CH_2CH_2OH radicals, respectively. A ratio acetaldehyde:vinyl alcohol of 4±1:1 was found by best fitting the experimental m/z 44 PES curve with the following equation

$$\mathrm{PES(m/z = 44@11\,eV)} = \mathrm{c1}\cdot\sigma_{\mathrm{11eV,acetaldehyde}}\cdot\mathrm{PES_{acetaldehyde}} + \mathrm{c2}\cdot\sigma_{\mathrm{11eV,vinylalcohol}}\cdot\mathrm{PES_{vinylalcohol}} \quad (1)$$

where c1 and c2 are constants, $\sigma_{\mathrm{11eV,acetaldehyde}}$ and $\sigma_{\mathrm{11eV,vinyl\ alcohol}}$ the photoionization cross-sections of the two compounds at 11 eV, and $\mathrm{PES_{acetaldehyde}}$ and $\mathrm{PES_{vinyl\ alcohol}}$ the corresponding experimental photoelectron spectra.

Integration of the temporal profiles in Fig. 10 was also used to estimate the ratios between the concentrations of the main products which reflect the branching ratios for the fuel decomposition pathways. As discussed above, the experimental profiles in Fig. 10 are affected by the change in pressure inside the spectrometer chamber. This may introduce some additional uncertainty into the following analysis although this is minimized by considering the ratios of species concentrations. The ratio C_2H_4:CH_3CHO:CH_2O between the integrated areas for the different species profiles from the simulations is 54:36:10 while the experimental value is 59:35:5 after removing the contribution from vinyl alcohol. The experimental values were obtained from Eq. 2 which relates the signal magnitude from a species (S_i) to the concentration (X_i), the photoionization cross-section at a particular photon energy (σ_{xxeV}) and mass discrimination factor (M_d).

$$S_i\,\alpha\,X_i\cdot\sigma_{\mathrm{xxeV}}\cdot M_d \quad (2)$$

where the constant of proportionality represents a collection of instrument specific constants independent of mass. The $\sigma_{\mathrm{11.0eV}}$ are 8.1 Mb [72], 7.9 Mb [73], and 9.6 Mb [74] for ethylene, acetaldehyde, and formaldehyde, respectively. In this work, we assume that M_d is unity for all species as they have not been determined for this apparatus. This introduces a small error into the calculation of concentrations, but based on Cool et al. [75] it will be small for the range m/z 28 to m/z 44 (ethylene to acetaldehyde). Considering the experimental uncertainties especially in the integration of the formaldehyde profile as well as the fact that the CRECK model was not validated against data obtained at similar conditions to those implemented in the current work, the agreement between the simulation and the experimental ratios is good.

To summarize the achievements presented in this section, the experimental results have demonstrated that accurate photoelectron spectra can be obtained from HRRST/i^{2}PEPICO experiments, and these are of sufficient quality to identify the main isomer contributing to a peak in the mass spectrum. Furthermore, the resulting pseudo-concentration/time histories for several species were obtained which allowed relative concentrations and branching ratios to be derived. The S/N is not sufficient to obtain accurate PESs nor temporal profiles for the minor peaks observed in this initial

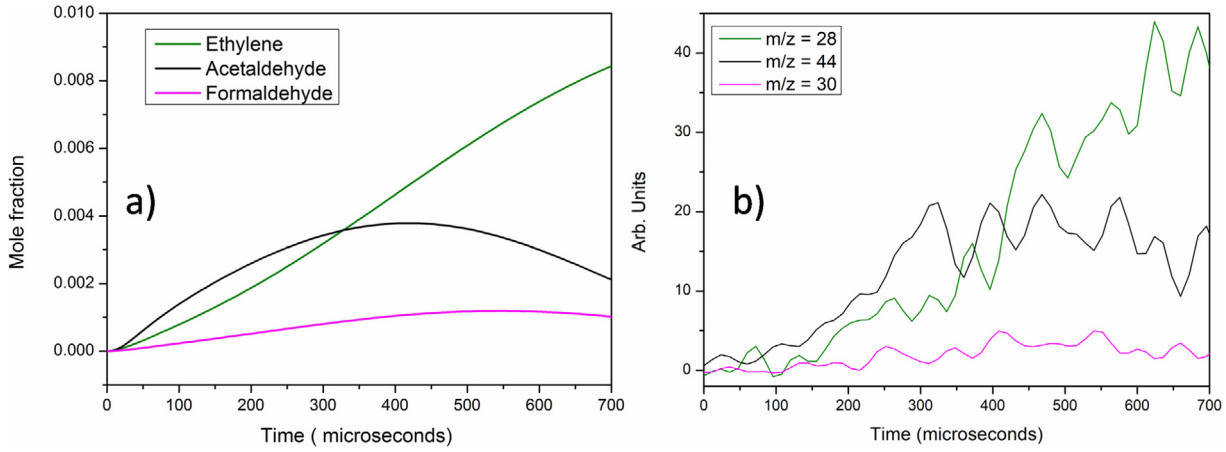

Fig. 10. Time histories for ethylene and m/z 28 (green), acetaldehyde and m/z 44 (black) and formaldehyde and m/z 30 (pink). a) Simulations with CRECK model [70]; b) experimental profiles.

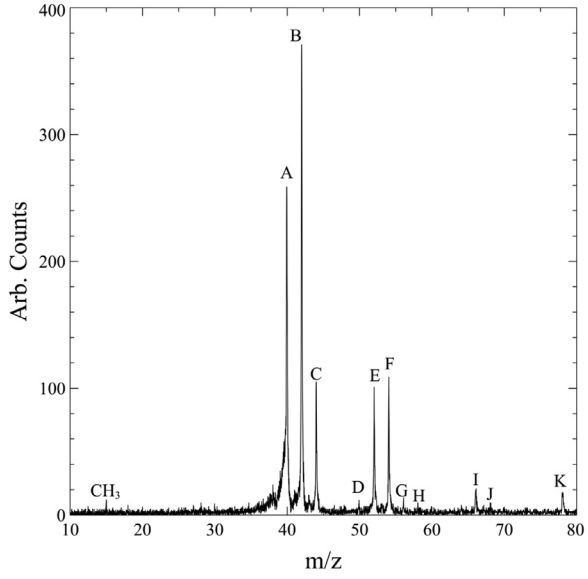

Fig. 11. The mass spectra obtained for $T_{5,mean}$ = 1234 K, $P_{5,mean}$ = 7.5 bar, 2.7% ethanol in argon. A: allene, B: propene/ketene, C: vinyl alcohol, D: mass 50, E: vinylacetylene, F: 1,3-butadiene (possible contribution from 1,2-butadiene), G: m/z 56. H= m/z 58, I: cyclopentadiene, J: m/z 68, K: benzene. Photon energy 10.0 eV.

set of experiments. In subsequent sections, we present some methods by which the S/N was improved for minor peaks, although further improvements will be a focus of ongoing studies. Moreover, the addition of an internal standard will allow quantitative measurements of concentration which will also clarify aspects related to detection limit, sensitivity, and dynamic range of the technique.

3.1.2. Low temperature, 10.0 eV photon energy

The second set of experiments was conducted at similar T_5 and P_5 ($T_{5,avg}$ = 1234 K, $P_{5,avg}$ = 7.5 bar) to the initial experiments but with a photon energy of 10.0 eV instead of 11.0 eV. This lower ionization energy suppressed the major peaks ethanol and ethylene, allowing more sensitive detection of minor products with ionization energies less than 10 eV, for example aromatics. The number of experiments was also increased from 15,000 to 27,000 to improve the S/N ratio for the small intermediates. The mass spectrum from the 27,000 experiments integrated over a total time of 7.8 ms (1.25 ms pre-shock, 6.55 ms post-shock) is given in Fig. 11. As expected, the mass spectrum is quite different from the one presented in Fig. 6. The primary differences are the absence of peaks at m/z 45, 46, and 28 and the appearance of additional peaks which could not be observed before. Of particular note is m/z 15, which corresponds to methyl radical, indicating radicals can be detected, a considerable achievement in these early experiments considering the low concentrations of such species. The presence of CH_3 is also indicative of the decomposition of ethanol through reaction 2. Other new identified species include cyclopentadiene (m/z 66) and benzene (m/z 78), although currently the contributions of isomers (cyclopropylacetylene, m/z 66 and 1,2-hexadiene-3-yne, m/z 78) to these peaks cannot be excluded, see for example Fig. S12 in the supplementary material. Minor peaks at m/z 50, 56, 58, and 68 could also be detected, but the S/N for these peaks is too small for definitive identification of species from the PES.

From the experiments at 11.0 eV, several mass peaks were assigned to a dominant isomer e.g. m/z 44 – acetaldehyde. Reducing the photon energy to 10.0 eV, below the IE of acetaldehyde, allowed other isomers of m/z 44 to be better identified for which only small features could be observed in the experimental PES at 11 eV. The isomers of m/z 44 considered were acetaldehyde, ethylene oxide, and vinyl alcohol. These have very different photoelectron spectra and as mentioned in Section 3.1.1, acetaldehyde was identified as the main contributor to the m/z 44 peak because of the good correspondence between the positions of the two peak maxima, as well as between the relative ratio of the peak heights (Fig. 12a for photon energy of 11 eV). The ionization energies of acetaldehyde and ethylene oxide are 10.24 eV and 10.57 eV [76], respectively, thus they do not contribute to the mass 44 peak in Fig. 11. Nevertheless, a peak at m/z 44 is present in Fig. 11 and the PES corresponds to vinyl alcohol (Fig. 12b). These results confirm the formation of vinyl alcohol as described in Section 3.1.1 and provide better definition of the corresponding PES.

Similarly, analysis of the 10.0 eV data confirmed that m/z 40 is composed of allene and propyne, the later being dominant in the 11.0 eV data (Fig. S9 and S11). The photoelectron spectrum of allene contains three main peaks at 9.69 eV, 9.93 eV, and 10.02 eV (not detectable at 10.0 eV) [35]. With a photon energy of 10.0 eV, the PES for m/z 40 is quite noisy because the ionization threshold for allene is very close to 10.0 eV, and $\sigma_{10.0eV}$ is small, but the main peak at 9.93 eV in the allene PES is well matched (Fig. S11). A small experimental peak at 10.02 eV is also observed at 11.0 eV in correspondence with the vertical ionization energy of allene (Fig. S9). Experiments at slightly higher photon energies than this ionization energy, e.g. 10.2 eV, would improve the m/z 40 PES and the identification of the profile for allene. These examples serve to

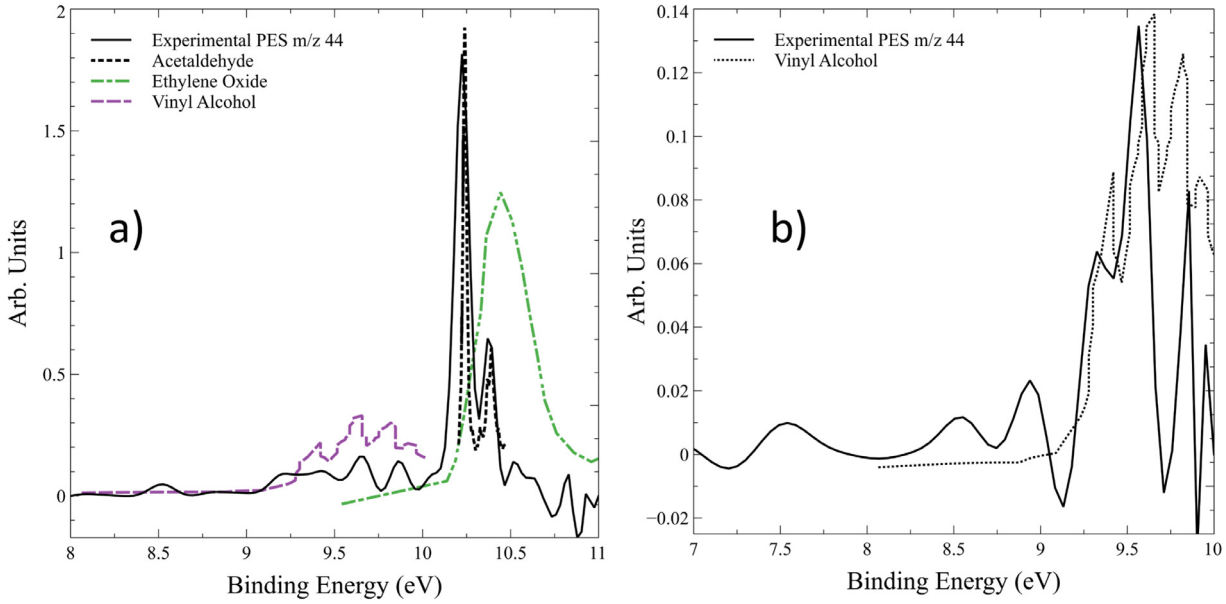

Fig. 12. Photoelectron spectra for m/z 44 (experimental), acetaldehyde [35], ethylene oxide [76] and vinyl alcohol [35]. Photon energy equal to a) 11.0 eV, b) 10.0 eV.

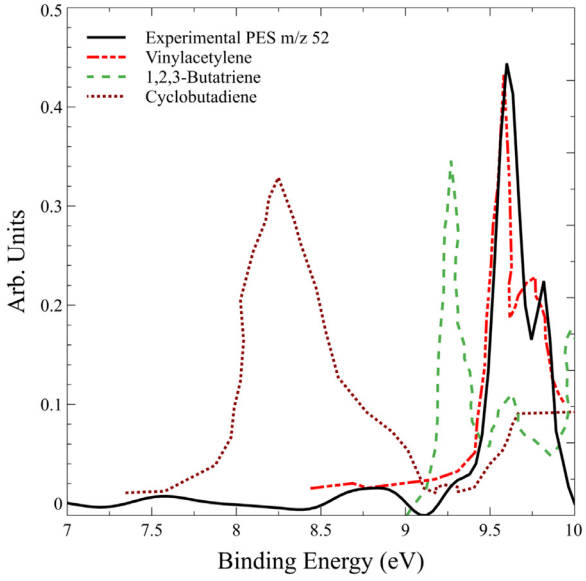

Fig. 13. Photoelectron spectra for m/z 52 (experimental), vinylacetylene [63], 1,2,3-butatriene [64], and cyclobutadiene [65]. Photon energy equal to 10.0 eV.

further demonstrate the capability of the HRRST/i^{2}PEPICO to identify mixed isomers by selecting appropriate photon energies.

Several products identified in Fig. 6 (11.0 eV) have ionization energies below 10.0 eV and the lower ionization energies generally resulted in much better resolution of the corresponding PESs. For example, in Fig. 8 the 11.0 eV PES for m/z 52, was presented. It consisted of broad peaks that did not capture details of the features of the literature PES of vinylacetylene. Reducing the ionization energy to 10.0 eV, eliminates the features between 10.5 and 11 eV, thus removing some detail from the PES. However, this loss is offset by resolving the two peaks at lower binding energies, that correspond to features in the literature PES for vinylacetylene, Fig. 13, and these allow for unambiguous assignment of m/z 52. It is interesting to compare the higher quality PES in Fig. 13 with Fig. 8 and note that a reasonably certain assignment of m/z 52 as vinylacetylene could be made based solely on Fig. 8 and the location of the maxima in the PES. The shoulder at 9.2 eV in Fig. 8 is mainly an artifact due to low sensitivity and the necessity of binning to recover the PES. This suggests that in cases where it is not possible to improve the PES, even a low resolution one may be sufficient. Furthermore, chemical kinetic modeling, where available and reliable, can be used judiciously to select isomers as candidates for a particular mass. Similar considerations apply to m/z 42, where a significant improvement in the definition of the PES was obtained in the lower photon energy experiments, although identification between propene and ketene was still not possible (Figs. S9 and S11).

The data presented in Sections 3.1.1 and 3.1.2 demonstrate that for a complex chemical system there is unlikely to be a single photon energy at which all of the desired data will be obtained. If it is necessary to identify species such as ethylene and ethanol, experiments have to be performed at relatively high ionization energies and it will be necessary to perform additional experiments at lower energies to target other species. The combined datasets provide considerably more insight than a study at a single ionization energy.

3.1.3. High temperature, 10.0 eV photon energy

As seen in the results of Sections 3.1.1 and 3.1.2, the temperature behind the reflected shock wave was not suitable for the formation of large amounts of PAHs. For example, benzene was the only aromatic species observed. In order to test the capability of the HRRST-i^{2}PEPICO system to measure large multi-ring structures, the experimental temperature was increased. The photon energy was kept at 10.0 eV to avoid masking of low concentration species by ethanol. A set of 32,000 experiments with $T_{5,mean}$ = 1525 K, σ = 55 K, and $P_{5,mean}$ = 7.5 bar, σ = 0.2 bar ($P_{5,mean}$ / $P_{1,mean}$ ~ 37) was carried out to obtain the mass spectrum shown in Fig. 14. Compared to the lower temperature experiments, numerous additional peaks were observed. These included PAHs of m/z up to 152 as well as various small species. Some of these products are common to Section 3.1.2 including methyl radical, vinyl alcohol, cyclopentadiene, vinylacetylene, allene, propene/ketene, and the features of the PESs are also very similar. At higher temperatures, a second radical was found, propargyl (m/z 39) in addition to methyl. Other linear compounds that were detected include 1,3-pentadiyne (m/z 64, Fig. S14), the C_6H_4 isomers (E)- and (Z)-1,5-hexadyine-3-yne (m/z 76, Fig. S15), and triacetylene (m/z 74, Fig. S15). The peak at m/z 76 may additionally contain a contribution from *o*-benzyne

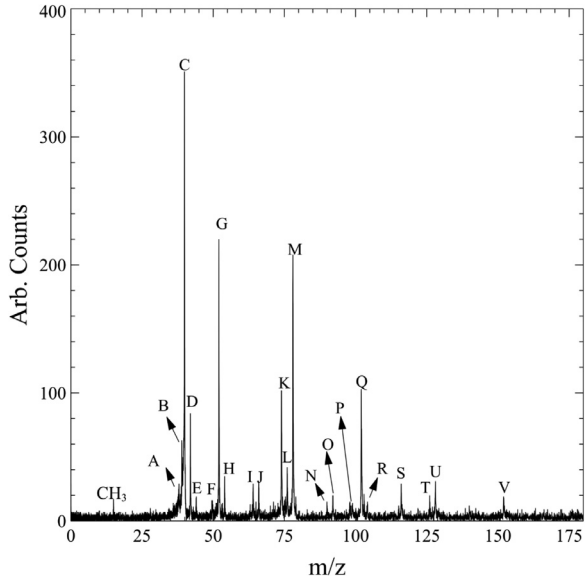

Fig. 14. The mass spectrum obtained for $T_{5,mean}$ = 1525 K, $P_{5,mean}$ = 7.5 bar, 2.7% ethanol in argon. A: m/z 38, B: propargyl radical, C: allene, D: propene/ketene, E: vinyl alcohol, F: m/z 50, G: vinylacetylene, H: 1,3 butadiene/2-butyne, I: 1,3-pentadiyne, J: cyclopentadiene, K: triacetylene, L: m/z 76, M: benzene, N: m/z 90, O: m/z 92, P: m/z 98, Q: phenylacetylene, R: styrene, S: indene/p-methylphenylacetylene, T: m/z 126, U: m/z 128, V: m/z 152. Photon energy 10.0 eV.

as the experimental PES shows a peak that corresponds to one of the reported ionization peak values for this diradical intermediate (9.83 eV [77]). Unfortunately, a second peak that would be expected from *o*-benzyne at 9.57 eV is indistinguishable from the peak corresponding to the 1,5-hexadyine-3-yne isomers. To confirm the presence of *o*-benzyne it would be necessary to improve the PES through more experiments or by increasing the number of molecules entering the ion source every shock

Features corresponding to the single-ring aromatic compounds, benzene (m/z 78), phenylacetylene (m/z 102), and styrene (m/z 104) are well resolved. The photoelectron spectrum of m/z 78 is presented in Fig. 15a along with the PES for selected C_6H_6 isomers including benzene. For clarity, we didn't plot the PES for all the possible isomers but only the ones which have reasonable similarities to the experimental PES. Compared to lower temperature conditions where the m/z 78 peak was small (Fig. 11), the m/z 78 signal in the higher temperature experiments is much larger with better S/N resulting in better resolution in the experimental PES. In a recent work on a low pressure premixed sooting flame [33], m/z 78 was assigned to a mixture of benzene and fulvene based on the comparison between convolved peaks and the experimental PES. Similar attempts were made here to assign the shoulder in m/z 78 to fulvene but it was not sufficiently resolved. In addition, the presence of fulvene would create a peak in Fig. 15a at around 8.5 eV which is not observed. Experiments at 8.7–9 eV would clarify the dilemma. Fig. 15b shows the excellent correspondence between peaks observed in the PES for m/z 102 and the literature PES for phenylacetylene [83].

Concerning larger PAH products, peaks were observed for m/z 116, 126, 128, and 152. The S/N ratio for these peaks is quite low, so the corresponding PES are not well resolved and a larger number of experiments would be required for accurate species identification. However, it is possible to use these low resolution PESs to reduce the number of possible isomers contributing to the PES which is almost as valuable as positively identifying contributors to the spectrum. For example, for m/z 116 the experimental PES is shown in Fig. 16 along with those of selected isomers. It is evident that only three isomers, indene, phenylpropadiene, and *p*-methylphenylacetylene, may be present in the observed PES. This example shows that even for compounds present in small concentrations, such as the PAHs, and for which the photoelectron spectra are not well defined, the PES curves may provide useful information to aid the identification of possible species among various isomers. Both PES and total ionization (PIE) curves can be used to distinguish isomers. However, the PIE curves are generally a less sensitive method because they are based upon the integral of photoelectron spectra over photon energies.

3.2. Experiments with low ethanol mole fractions (0.0025)

This part of the study was conducted with the goal of testing the feasibility of using much lower reagent concentrations than in Section 3.1. Experiments with highly-diluted mixtures are pre-

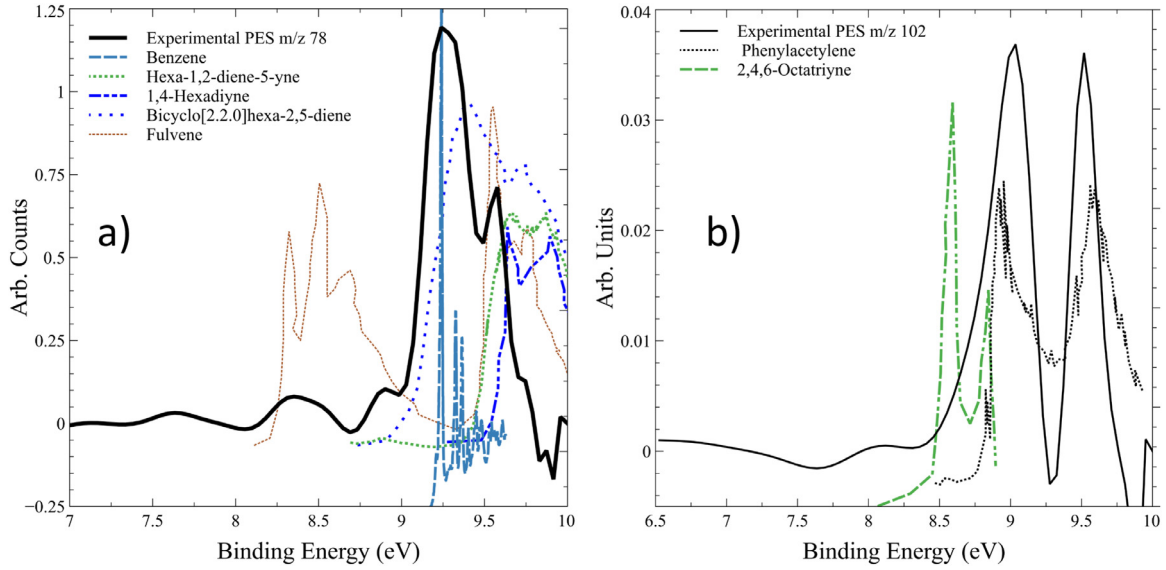

Fig. 15. a) Photoelectron spectra for m/z 78 (experimental), benzene [78], fulvene [79], 1,2-hexadiene-5-yne [80], 1,4-hexadiyne [81], and bicyclo[2.2.0]hexa-2,5-diene [82]. b) Photoelectron spectra for m/z 102 (experimental), phenylacetylene [83], and 2,4,6-octatriyne [84].

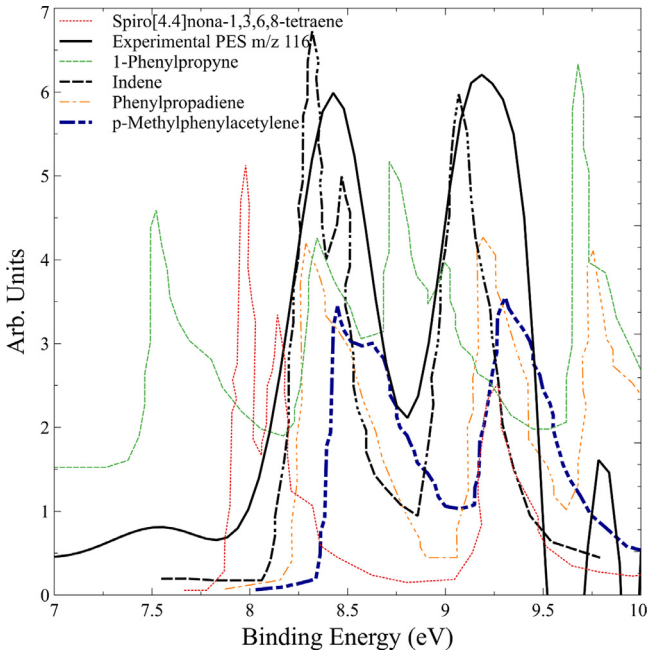

Fig. 16. Photoelectron spectra for m/z 116 (experimental) and selected isomers (indene [85], 1-phenylpropyne [86], spiro[4.4]nona-1,3,6,8-tetraene [86], phenylpropadiene [87], p-methylphenylacetylene [88]).

ferred for kinetic analyses of isolated reaction mechanisms and reaction rate parameters and branching ratios. Here the ethanol concentration was reduced by approximately a factor of 10 to 0.25%. Reducing the concentration would of course reduce signal levels. To obtain sufficient signal with a reasonable number of experiments, the components of the MBS were changed and a robust method of axially aligning the nozzle and first skimmer and maintaining their separation was implemented, details are given in the supplementary material. Skimmer 1 was replaced by a Beam Dynamics model-1 skimmer with a 1 mm orifice (the original was model-2 with 0.5 mm orifice), while the nozzle was changed to a smaller orifice of 0.3 mm. The separation of the nozzle and skimmer was fixed at 10 nozzle diameters where maximum cooling from expansion of the supersonic jet is achieved and the jet density is high. The smaller nozzle was necessary to avoid excess pressure in the spectrometer chamber due to the increased flux through the larger orifice of skimmer 1. Skimmer 2 was not changed but the separation between skimmers 1 and 2 was decreased. The net effect of the changes to the MBS components and their alignment was to increase the flow from the shock tube to the interaction region of the spectrometer while maintaining safe operating pressures. For this set of experiments, the upstream variable aperture which defines the transverse size of the photon beam entering the ionization chamber was also narrowed to around 65% in order to obtain a better spatial resolution at the expense of a somewhat reduced photon flux. In this case, the resolution was improved from 25 to 15 meV.

The modified set-up was used to run around 9,000 experiments with a photon energy of 11.0 eV as in Section 3.1.1, with $T_{5,mean}$ of 1354 K, σ = 23 K, and $P_{5,mean}$ = 6.2 bar, σ = 0.1 bar. The mass spectrum corresponding to the signal integrated over 7.8 ms (0.75 ms pre-shock and 7.05 ms post-shock) is presented in Fig. 17 along with the mass spectrum from Section 3.1.1 (2.7% ethanol). The S/N is moderately lower at diluted conditions, but the peaks are still well-defined and resolved. However, the initial con-

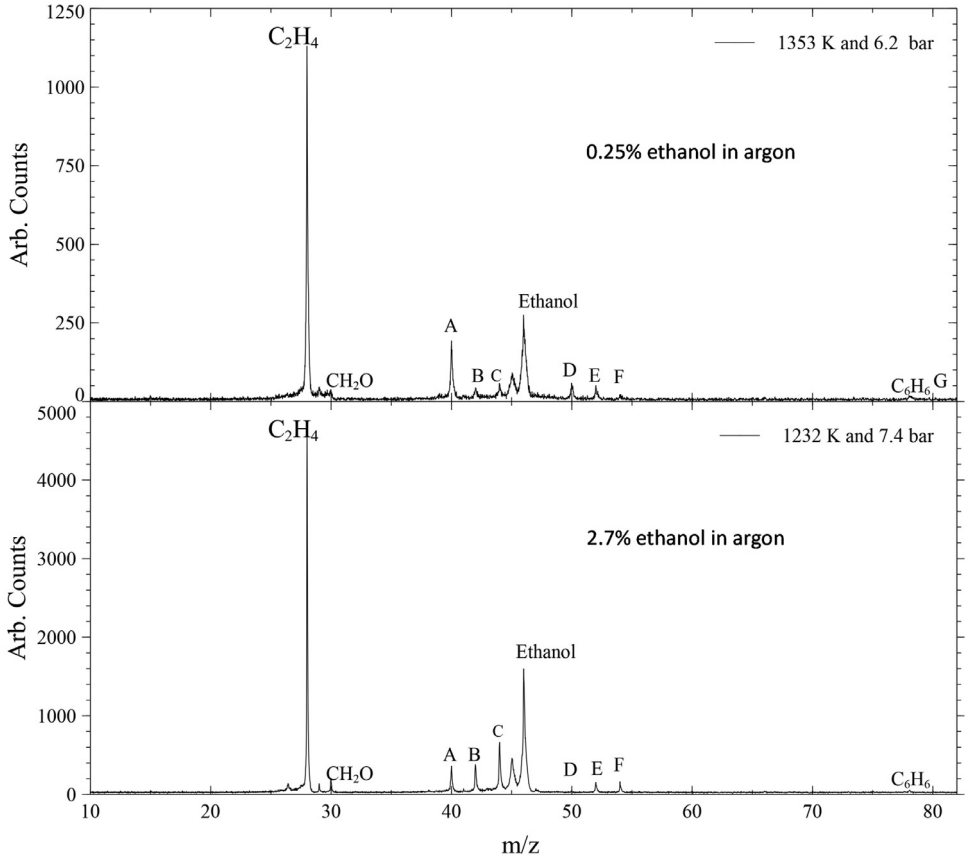

Fig. 17. (Top) Mass spectrum obtained with 0.25% ethanol in argon. A: propyne, B: propene/ketene, C: acetaldehyde+ vinyl alcohol, D: diacetylene, E: vinylacetylene, F: 1,3 butadiene (possible contribution from 1-butyne). (Bottom) Mass spectrum obtained with 2.7% ethanol, for comparison. Photon energy 11.0 eV.

centration of ethanol was a factor of 10 lower than the earlier experiments and only 9,000 experiments were performed as opposed to 15,000. There is a slight difference in the ratios between the different peak heights which can be mainly attributed to the difference in temperature and pressure conditions between the two cases. For the dilute mixtures, the experimental ratios between the integrated time-history profiles for ethylene, acetaldehyde, and formaldehyde over 700 µs are 0.69:0.06:0.25. Simulations were performed with the CRECK model at $T = 1354$ K, $P = 6.2$ bar, and constrained pressure, and the results of the integrated species profiles give 0.82:0.08:0.1 in reasonable agreement with the experimental values. Concerning the photoelectron spectra, they are similar to those obtained in Section 3.1.1. An exception is vinylacetylene, for which the second peak at around 10.5 eV is not well resolved in the experimental PES of m/z 52. Similarly, m/z 54 is also not well resolved, but the corresponding peak is very small in this case. On the other hand, the m/z 50 peak, which is much larger than in Fig. 6, can be easily attributed to diacetylene. Overall, the improved alignment resulted in successful experiments with a highly diluted reagent mixture. Furthermore, the quality of the data obtained were almost as good as those obtained with higher fuel concentrations but with far fewer experiments. The reduced time to get good S/N in the mass spectra gives flexibility in planning future experiments. For example, a broader range of experimental conditions could be explored or attention focused on one set of conditions and high-resolution results obtained, as appropriate.

5. Conclusions

Results from the first ever experiments with a shock tube and a synchrotron-based photoelectron photoion coincidence spectrometer were presented and a number of aspects of the work are highlighted here:

(1) A new miniature high-repetition rate shock tube (ICARE-HRRST) was developed for installation in the SAPHIRS chamber at the beamline DESIRS of the SOLEIL synchrotron to allow the i^{2}PEPICO technique to be used. The performance of the shock tube was excellent and over tens of thousands of experiments very reproducible reaction conditions were produced at repetition rates up to 1.5 Hz. Due to the reproducibility, signal averaging of the spectral data could be performed with confidence.

(2) These experiments represent the first use of an electron/ion coincidence spectrometer like DELICIOUS-III with a non-pseudo-steady state reactor such as the ICARE-HRRST. The pulsed nature of the experiments and the large pressure due to the reflected shock wave presented a number of challenges including low duty cycles relative to steady state sources and large changes in pressures in the spectrometer during each experiment. Nevertheless, the high collection efficiency of both electrons and ions and the fast acquisition time of the fixed-photon energy VMI electron spectrometer allowed mass spectra, photoelectron spectra, and time and mass resolved spectra to be acquired.

(3) The detailed spectral information was used to probe aspects of ethanol pyrolysis under both sooting and non-sooting conditions. In the different regimes various aspects of the pyrolysis of ethanol could be investigated. At lower temperatures it was possible to quantify branching ratios related to the initial steps of ethanol dissociation. Whereas, the high temperature experiments cast light on the formation of aromatic species and the early stages of PAH growth. A critical part of interpreting data from both regimes was having the photoelectron spectra as well as the mass spectra. These two pieces of information allowed contributions of isomeric species to be either quantified (fuel and major products) or qualitatively assessed (minor products); although for many compounds, the low S/N ratio did not permit the identification of accurate PE spectra and temporal profiles.

(4) These experiments were the first of their kind and thus also provided a unique opportunity for developing the methodology and guiding the design of future experimental campaigns. In the course of experiments several improvements were made to the coupling of the ICARE-HRRST and DELICIOUS-III. However, while these greatly improved the S/N they also revealed a number of additional areas for future improvements including further optimization of the nozzle and skimmer combinations and separations to maximize signal while minimizing pressure pulses in the spectrometer. To obtain kinetic data it will be necessary to develop a suitable internal standard to correct the temporal profiles for pressure changes. This is a focus of ongoing work.

(5) For HRRST/i^{2}PEPICO experiments, the selection of ionization energy is critical, and accuracy and signal levels trade off in non-intuitive ways. For this reason, compromises will have to be made in order to perform accurate measurements for species in low concentrations such as radicals or large PAH against being able to observe species present at high ionization energies. It is likely that as more experience is gained with this method and anticipated signal levels can be better predicted and simulated *a priori*, reaction conditions and spectrometer settings can be properly optimized for efficient data collection with respect to number of experiments.

Overall, these initial experiments were very successful considering that this was the first attempt to couple these two complex techniques. The results indicate the potential for detailed explorations of mechanisms and kinetics at temperatures and pressures relevant to practical combustion devices using the well-defined reaction conditions characteristic of shock tubes and the detailed spectral temporal information from i^{2}PEPICO.

Declaration of Competing Interest

The authors declare that they have no known competing financial interests or personal relationships that could have appeared to influence the work reported in this paper.

Acknowledgements

This project has received funding from the European Research Council (ERC) under the European Union's Horizon 2020 research and innovation program (grant agreement No. 756785). We are grateful to the whole SOLEIL staff for provision of beamtime under project 20190102**.** Robert Simon Tranter acknowledges support from the U.S. Department of Energy, Office of Basic Energy Sciences, Division of Chemical Sciences, Geosciences, and Biosciences through Argonne National Laboratory and the Argonne/Sandia Consortium on High Pressure Combustion Chemistry. Argonne is a U.S. Department of Energy laboratory managed by UChicago Argonne, LLC, under contract DE-AC02-06CH11357.

Supplementary materials

Supplementary material associated with this article can be found, in the online version, at doi:10.1016/j.combustflame.2020.11.035.

References

[1] P. Vieille, Sur les discontinuites produites par la détente brusque de gas comprimes, Comptes Rendus 129 (1899) 1228–1230.
[2] P. Vieille, Etude sur les roles des discontinuites dans les phenomenes de propagation, Mémorial des Poudres et Salpêtres 10 (1899) 177–260.
[3] G. Ben-Dor, O. Igra, A. Lifshitz (Eds.), Handbook of Shock Waves, Academic Press, New York, 2001.
[4] A. Lifshitz (Ed.), Shock Waves in Chemistry, Dekker, New York, 1981.
[5] J.H. Kiefer, S.S. Kumaran, S. Sundaram, Vibrational relaxation, dissociation, and dissociation incubation times in norbornene, J. Chem. Phys. 99 (1993) 3531–3541.
[6] J.H. Kiefer, R. Sathyanarayana, Vibrational relaxation and dissociation in the perfluoromethyl halides, CF3Cl, CF3Br, and CF3I, Int. J. Chem. Kinet. 29 (1997) 705–716.
[7] R.S. Tranter, A. Raman, R. Sivaramakrishnan, K. Brezinsky, Ethane oxidation and pyrolysis from 5 bar to 1000 bar: experiments and simulation, Int. J. Chem. Kinet. 37 (2005) 306–331.
[8] M.F. Campbell, T. Parise, A.M. Tulgestke, R.M. Spearrin, D.F. Davidson, R.K. Hanson, Strategies for obtaining long constant-pressure test times in shock tubes, Shock Waves 25 (2015) 651–665.
[9] R.S. Tranter, K. Brezinsky, D. Fulle, Design of a high-pressure single pulse shock tube for chemical kinetic investigations, Rev. Sci. Instrum. 72 (2001) 3046–3054.
[10] E.L. Petersen, R.K. Hanson, Nonideal effects behind reflected shock waves in a high-pressure shock tube, Shock Waves 10 (2001) 405–420.
[11] D.F. Davidson, D.R. Haylett, R.K. Hanson, Development of an aerosol shock tube for kinetic studies of low-vapor-pressure fuels, Combust. Flame 155 (2008) 108–117.
[12] K.-Y. Lam, Z. Hong, D.F. Davidson, R.K. Hanson, Shock tube ignition delay time measurements in propane/O_2/argon mixtures at near-constant-volume conditions, Proc. Combust. Inst. 33 (2011) 251–258.
[13] D. Nativel, S.P. Cooper, T. Lipkowicz, M. Fikri, E.L. Petersen, C. Schulz, Impact of shock-tube facility-dependent effects on incident-and reflected-shock conditions over a wide range of pressures and Mach numbers, Combust. Flame 217 (2020) 200–211.
[14] M. Yamauchi, H. Matsui, M. Koshi, K. Tanaka, S. Tamaki, H. Tanaka, Shock tube studies on the radical emission spectra by use of an imaging spectrometer, Bunko Kenkyu 36 (1987) 388–394.
[15] R.S. Tranter, B.R. Giri, A diaphragmless shock tube for high temperature kinetic studies, Rev. Sci. Instrum. 79 (2008) 094103.
[16] B.R. Giri, J.H. Kiefer, H. Xu, S.J. Klippenstein, R.S. Tranter, An experimental and theoretical high temperature kinetic study of the thermal unimolecular dissociation of fluoroethane, Phys. Chem. Chem. Phys. 10 (2008) 6266–6273.
[17] R.S. Tranter, P.T. Lynch, A miniature high repetition rate shock tube, Rev. Sci. Instrum. 84 (2013) 094102.
[18] G.A. Garcia, X. Tang, J.F. Gil, L. Nahon, M. Ward, S. Batut, C. Fittschen, C.A. Taatjes, D.L. Osborn, J.C. Loison, Synchrotron-based double imaging photoelectron/photoion coincidence spectroscopy of radicals produced in a flow tube: OH and OD, J. Chem. Phys. 142 (2015) 164201.
[19] C.A. Taatjes, N. Hansen, D.L. Osborn, K. Kohse-Höinghaus, T.A. Cool, P.R. Westmoreland, "Imaging" combustion chemistry via multiplexed synchrotron-photoionization mass spectrometry, Phys. Chem. Chem. Phys. 10 (2008) 20–34.
[20] R.A. Shaik, A.L. Kastengren, R.S. Tranter, P.T. Lynch, Temporally and spatially resolved X-ray densitometry in a shock tube, Combust. Flame (2020) https://doi.org/10.1016/j.combustflame.2020.09.035.
[21] P.T. Lynch, T.P. Troy, M. Ahmed, R.S. Tranter, Probing combustion chemistry in a miniature shock tube with synchrotron VUV photo ionization mass spectrometry, Anal. Chem. 87 (2015) 2345–2352.
[22] J.B. Randazzo, R. Sivaramakrishnan, A.W. Jasper, T. Sikes, P.T. Lynch, R.S. Tranter, An experimental and theoretical study of the high temperature reactions of the four butyl radical isomers, Phys. Chem. Chem. Phys. (2020) https://doi.org/10.1039/D0CP02404J.
[23] C. Banyon, T. Sikes, R.S. Tranter, Reactions of propyl radicals: a shock tube–VUV photoionization mass spectrometry study, Combust. Flame (2020) https://doi.org/10.1016/j.combustflame.2020.10.024.
[24] S. Wang, D.F. Davidson, R.K. Hanson, Shock tube and laser absorption study of CH_2O oxidation via simultaneous measurements of OH and CO, J. Phys. Chem. A 121 (2017) 8561–8568.
[25] R.M. Spearrin, S. Li, D.F. Davidson, J.B. Jeffries, R.K. Hanson, High-temperature iso-butene absorption diagnostic for shock tube kinetics using a pulsed quantum cascade laser near 11.3μm, Proc. Comb. Inst. 35 (3) (2015) 3645–3651.
[26] B.R. Giri, J.H. Kiefer, R.S. Tranter, Shock tube/time-of-flight mass spectrometer for high temperature kinetic studies, Rev. Sci. Instrum. 78 (2007) 034101.
[27] R.D Kern, H.J. Singh, Q. Zhang, in: G. Ben-Dor, O. Igra, T. Elperin, A. Lifshitz (Eds.), Mass Spectrometric Methods for Chemical Kinetics in Shock Tubes, Handbook of Shock Waves, Chemical Reactions in Shock Waves and Detonations;, Vol. 3 (2001), pp. 1–27. Ch. 16.1Pg.
[28] L. Weiser, I. Weber, M. Olzmann, Pyrolysis of furan and its methylated derivatives: a shock-Tube/TOF-MS and modeling study, J. Phys. Chem. A 46 (2019) 9893–9904.
[29] P. Sela, Y. Sakai, H.S. Choi, J. Herzler, M. Fikri, C. Schulz, S. Peukert, High-temperature unimolecular decomposition of diethyl ether: shock-tube and theory studies, J. Phys. Chem. A 123 (2019) 6813–6827.
[30] A. Schweig, H. Vermeer, U. Weidner, A photoelectron spectroscopic study of keto-enol tautomerism in acetylacetones-a new application of photoelectron spectroscopy, Chem. Phys. Lett. 26 (1974) 229–233.
[31] J. Pieper, S. Schmitt, C. Hemken, E. Davies, J. Wullenkord, A. Brockhinke, J. Krüger, G.A. Garcia, L. Nahon, A. Lucassen, W. Eisfeld, K. Kohse-Höinghaus, Isomer identification in flames with double-imaging photoelectron/photoion coincidence spectroscopy (i2PEPICO) using measured and calculated reference photoelectron spectra, Zeitschrift für Physikalische Chemie 232 (2018) 153–187.
[32] J. Krüger, G.A. Garcia, D. Felsmann, K. Moshammer, A. Lackner, A. Brockhinke, L. Nahon, K. Kohse-Höinghaus, Photoelectron–photoion coincidence spectroscopy for multiplexed detection of intermediate species in a flame, Phys. Chem. Chem. Phys. 16 (2014) 22791–22804.
[33] X. Mercier, A. Faccinetto, S. Batut, G. Vanhove, D.K. BoŽanić, H.R. Hróðmarsson, G.A. Garcia, L. Nahon, Selective identification of cyclopentaring-fused PAHs and side-substituted PAHs in a low pressure premixed sooting flame by photoelectron photoion coincidence spectroscopy, Phys. Chem. Chem. Phys. 22 (2020) 15926–15944.
[34] M. Hoener, D. Kaczmarek, T. Bierkandt, A. Bodi, P. Hemberger, T. Kasper, A pressurized flow reactor combustion experiment interfaced with synchrotron double imaging photoelectron photoion coincidence spectroscopy, Rev. Sci. Instrum. 91 (2020) 045115.
[35] P. Oßwald, P. Hemberger, T. Bierkandt, E. Akyildiz, M. Köhler, A. Bodi, T. Gerber, T. Kasper, In situ flame chemistry tracing by imaging photoelectron photoion coincidence spectroscopy, Rev. Sci. Instrum. 85 (2014) 025101.
[36] J. Bourgalais, Z. Gouid, O. Herbinet, G.A. Garcia, P. Arnoux, Z. Wang, L.S. Tran, G. Vanhove, M. Hochlaf, L. Nahon, F. Battin-Leclerc, Isomer-sensitive characterization of low temperature oxidation reaction products by coupling a jet-stirred reactor to an electron/ion coincidence spectrometer: case of n-pentane, Phys. Chem. Chem. Phys. 22 (2020) 1222–1241.
[37] M.T. Baeza-Romero, F. Gaie-Levrel, A. Mahjoub, V. López-Arza, G.A. Garcia, L. Nahon, A smog chamber study coupling a photoionization aerosol electron/ion spectrometer to VUV synchrotron radiation: organic and inorganic-organic mixed aerosol analysis, Eur. Phys. J. D 70 (2016) 154–164.
[38] D.V. Chicharro, S.M. Poullain, L. Banares, H.R. Hrodmarsson, G.A. Garcia, J.C. Loison, Threshold photoelectron spectrum of the CH_2OO Criegee intermediate, Phys. Chem. Chem. Phys. 21 (2019) 12763–12766.
[39] X. Tang, X. Gu, X. Lin, W. Zhang, G.A. Garcia, C. Fittschen, J.C. Loison, K. Voronova, B. Sztáray, L. Nahon, Vacuum ultraviolet photodynamics of the methyl peroxy radical studied by double imaging photoelectron photoion coincidences, J. Chem. Phys. 152 (2020) 104301.
[40] P. Hemberger, J.A. van Bokhoven, J. Pérez-Ramírez, A. Bodi, New analytical tools for advanced mechanistic studies in catalysis: photoionization and photoelectron photoion coincidence spectroscopy, Catal. Sci. Technol. 10 (2020) 1975–1990.
[41] P. Hemberger, V.B.F. Custodis, A. Bodi, T. Gerber, J.A. van Bokhoven, Understanding the mechanism of catalytic fast pyrolysis by unveiling reactive intermediates in heterogeneous catalysis, Nat. Commun. 8 (2017) 1–9.
[42] L. Nahon, N. de Oliveira, G.A. Garcia, J.F. Gil, D. Joyeux, B. Lagarde, F. Polack, DESIRS: a state-of-the-art VUV beamline featuring high resolution and variable polarization for spectroscopy and dichroism at SOLEIL, J. Phys.: Conf. Ser. 425 (2012) 122004.
[43] X. Tang, G.A. Garcia, J.F. Gil, L. Nahon, Vacuum upgrade and enhanced performances of the double imaging electron/ion coincidence end-station at the vacuum ultraviolet beamline DESIRS, Rev. Sci. Instrum. 86 (2015) 123108.
[44] G.A. Garcia, B.K. Cunha de Miranda, M. Tia, S. Daly, L. Nahon, DELICIOUS III: a multipurpose double imaging particle coincidence spectrometer for gas phase vacuum ultraviolet photodynamics studies, Rev. Sci. Instrum. 84 (2013) 053112.
[45] R. Choudhary, Y. Peng, J. Shao, D.F. Davidson, R.K. Hanson, Multi-species time history measurements during ethanol pyrolysis behind reflected shock waves, 11th US National Combustion Meeting, 2019.
[46] J. Kiecherer, C. Bänsch, T. Bentz, M. Olzmann, Pyrolysis of ethanol: a shock–tube/TOF-MS and modeling study, Proc. Combust. Inst. 35 (2015) 465–472.
[47] J. Li, A. Kazakov, F.L. Dryer, Ethanol pyrolysis experiments in a variable pressure flow reactor, Int. J. Chem. Kinet. 33 (2001) 859–867.
[48] R. Sivaramakrishnan, M.C. Su, J.V. Michael, S.J. Klippenstein, L.B. Harding, B. Ruscic, Rate constants for the thermal decomposition of ethanol and its bimolecular reactions with OH and D: reflected shock tube and theoretical studies, J. Phys. Chem. A 114 (2010) 9425–9439.
[49] C.W. Wu, H. Matsui, N.S. Wang, M.C. Lin, Shock tube study on the thermal decomposition of ethanol, J. Phys. Chem. A 115 (2011) 8086–8092.
[50] M. Aghsaee, D. Nativel, M. Bozkurt, M. Fikri, N. Chaumeix, C. Schulz, Experimental study of the kinetics of ethanol pyrolysis and oxidation behind reflected shock waves and in laminar flames, Proc. Combust. Inst. 35 (2015) 393–400.
[51] J. Park, R.S. Zhu, M.C. Lin, Thermal decomposition of ethanol. I. Ab Initio molecular orbital/Rice–Ramsperger–Kassel–Marcus prediction of rate constant and product branching ratios, J. Chem. Phys. 117 (2002) 3224–3231.
[52] L. Xing, S. Li, Z. Wang, B. Yang, S.J. Klippenstein, F. Zhang, Global uncertainty analysis for RRKM/master equation based kinetic predictions: a case study of ethanol decomposition, Combust. Flame 162 (2015) 3427–3436.
[53] A.G. Vandeputte, L.B. Harding, Y. Georgievskii, S.J. Klippenstein, Roaming radical kinetics in the pyrolysis and combustion of ethanol, 8th U. S. National Combustion Meeting, 2013 Paper 070RK–157.
[54] R.A. Alpher, D.R. White, Flow in shock tubes with area change at the diaphragm section, J. Fluid Mech 3 (1958) 457–470.

[55] R.S. Tranter, T. Sikes, Solenoid actuated driver valve for high repetition rate shock tubes, Rev. Sci. Instrum. 91 (2020) 056101.
[56] P.T. Lynch, Note: An improved solenoid driver valve for miniature shock tubes, Rev Sci. Instrum. 87 (2016) 056110.
[57] A. Matsugi, A high-repetition-rate shock tube for transient absorption and laser-induced fluorescence studies of high-temperature chemical kinetics, Rev. Sci. Instrum. 91 (2020) 054101.
[58] D. Ceolin, G. Chaplier, M. Lemonnier, G.A. Garcia, C. Miron, L. Nahon, M. Simon, N. Leclercq, P. Morin, Rev. Sci. Instrum. 76 (2005) 043302.
[59] G.A. Garcia, L. Nahon, I. Powis, Two-dimensional charged particle image inversion using a polar basis function expansion, Rev. Sci. Instrum. 75 (2004) 4989–4996.
[60] J.L. Holmes, F.P. Lossing, Ionization energies of homologous organic compounds and correlation with molecular size, Org. Mass Spectrom. 26 (1991) 537–541.
[61] D.R. Miller, Atomic and molecular beam methods, in: G. Scoles (Ed) (Ed.), Atomic and Molecular Beam Methods, Oxford University Press, Oxford (1988), pp. 14–53.
[62] G.R. Branton, D.C. Frost, T. Makita, C.A. McDowell, I.A. Stenhouse, Photoelectron Spectra of Ethylene and Ethylene-d 4, J. Chem. Phys. 52 (1970) 802–806.
[63] P. Bruckmann, M. Klessinger, Photoelektronenspektren organischer verbindungen: III. Photoelektronenspektren acetylensubstituierter kleiner ringe, J. Electron Spectroscopy Related Phenomena 2 (1973) 341–354.
[64] F. Brogli, E. Heilbronner, E. Kloster-Jensen, A. Schmelzer, A.S. Manocha, J.A. Pople, L. Radom, The photoelectron spectrum of butatriene, Chem. Phys. 4 (1974) 107–119.
[65] J. Kreile, N. Münzel, A. Schweig, H. Specht, Uv photoelectron spectrum of cyclobutadiene. free cyclobutadiene stable up to high temperatures, Chem. Phys. Lett. 124 (1986) 140–146.
[66] G.A. Garcia, H. Soldi-Lose, L. Nahon, A versatile electron-ion coincidence spectrometer for photoelectron momentum imaging and threshold spectroscopy on mass selected ions using synchrotron radiation, Rev. Sci. Instrum. 80 (2009) 023102.
[67] V.K. Potapov, V.V. Sorokin, Kinetic energies of products of dissociative photoionization of molecules. I. Aliphatic ketones and alcohols, Khim. Vys. Energ. 6 (1972) 387–391.
[68] R.D. Kern, H.J. Singh, Q. Jhang, Mass spectrometric methods for chemical kinetics in shock tubes, in: G. Ben-Dor, O. Igra, A. Lifshitz(Eds.) (Eds.), Handbook of Shock Waves, 3, Academic Press, New York (2001), pp. 1–27. Chap. 16.
[69] R.S. Tranter, B.R. Giri, Shock tube/time-of-flight mass spectrometer for high temperature kinetic studies, Rev. Sci. Instrum. 78 (2007) 034101.
[70] W. Pejpichestakul, E. Ranzi, M. Pelucchi, A. Frassoldati, A. Cuoci, A. Parente, T. Faravelli, Examination of a soot model in premixed laminar flames at fuel-rich conditions, Proc. Combust. Inst. 37 (2019) 1013–1021.
[71] COSILABThe Combustion Simulation Laboratory, Rotexo GmbH & Co., KG, Haan, Germany, 2009 Version 3.3.2.
[72] J.C. Person, P.P. Nicole, Isotope effects in the photoionization yields and the absorption cross sections for ethylene and n-butane, J. Chem. Phys. 49 (1968) 5421–5426.
[73] T.A. Cool, K. Nakajima, T.A. Mostefaoui, F. Qi, A. McIlroy, P.R. Westmoreland, M.E. Law, L. Poisson, D.S. Peterka, M. Ahmed, Selective detection of isomers with photoionization mass spectrometry for studies of hydrocarbon flame chemistry, J. Chem. Phys. 119 (2003) 8356–8365.
[74] L.G. Dodson, L. Shen, J.D. Savee, N.C. Eddingsaas, O. Welz, C.A. Taatjes, D.L. Osborn, S.P. Sander, M. Okumura, VUV photoionization cross sections of HO_2, H_2O_2, and H_2CO, J. Phys. Chem. A 119 (2015) 1279–1291.
[75] T.A. Cool, A. McIlroy, F. Qi, P.R. Westmoreland, L. Poisson, D.S. Peterka, M. Ahmed, Photoionization mass spectrometer for studies of flame chemistry with a synchrotron light source, Rev. Sci. Instrum. 76 (2005) 094102.
[76] K. Johnson, I. Powis, C.J. Danby, A photoelectron—photoion coincidence study of acetaldehyde and ethylene oxide molecular ions, Chem. Phys. 70 (1982) 329–343.
[77] M.J.S. Dewar, T.P. Tien, Photoelectron spectrum of benzyne, J. Chem. Soc., Chem. Commun. 18 (1985) 1243–1244.
[78] L. Åsbrink, E. Lindholm, O. Edqvist, Jahn-Teller effect in the vibrational structure of the photoelectron spectrum of benzene, Chem. Phys. Lett. 5 (1970) 609–612.
[79] E. Heilbronner, R. Gleiter, H. Hopf, V. Hornung, A. De Meijere, Photoelectron-Spectroscopic Evidence for the Orbital Sequence in Fulvene and 3, 4-Dimethylene-cyclobutene, Helv. Chim. Acta 54 (1971) 783–794.
[80] P. Bischof, R. Gleiter, H. Hopf, F.T. Lenich, Photoelectron spectra of open chain C_6H_6 isomers, J. Am. Chem. Soc. 97 (1975) 5467–5472.
[81] F. Brogli, E. Heilbronner, J. Wirz, E. Kloster-Jensen, R.G. Bergman, K. Peter C. Vollhardt, A.J. Ashe III, The consequences of σ and π conjugative interactions in mono-, di-and triacetylenes. A photoelectron spectroscopic investigation, Helv. Chim. Acta 58 (1975) 2620–2645.
[82] G. Bieri, E. Heilbronner, T. Kobayashi, A. Schmelzer, M.J. Goldstein, R.S. Leight, M.S. Lipton, Dewar benzene and some of its derivatives. A photoelectron spectroscopic analysis, Helv. Chim. Acta 59 (1976) 2657–2673.
[83] J.P. Maier, D.W. Turner, Steric inhibition of resonance studied by molecular photoelectron spectroscopy. Part 2.—Phenylethylenes, J. Chem. Soc., Faraday Trans. 2 69 (1973) 196–206.
[84] C. Baker, D.W. Turner, High resolution molecular photoelectron spectroscopy. III. Acetylenes and aza-acetylenes, Proc. R. Soc. Lond. A 308 (1968) 19–37.
[85] J.H.D. Eland, C.J. Danby, Inner ionization potentials of aromatic compounds, Zeitschrift für Naturforschung A 23 (1968) 355–357.
[86] S. Elbel, K. Lienert, A. Krebs, H.T. Dieck, Photoelektronenspektren von Phenylethinen, I. Phenylethin-Mustersonde für Substituenteneffekte, Liebigs Annalen der Chemie 10 (1981) 1785–1797.
[87] W. Runge, W. Kosbahn, J. Kroner, The molecular structure of allenes and ketenes II [1] photoelectron spectra, absorption spectra, and CNDO/S-calculations of phenyl and methyl substituted Allenes, Berichte der Bunsengesellschaft für physikalische Chemie 79 (1975) 371–381.
[88] R. Griebel, G. Hohlneicher, F. Dörr, A photoelectron spectroscopic study of benzonitrile, ethynylbenzene and some of its substituted derivatives, J. Electron Spectros Relat Phenomena 4 (1974) 185–206.